

Stellar Populations of Ly α Emitting Galaxies in the HETDEX Survey I: An Analysis of LAEs in the GOODS-N Field

2 ADAM P. McCARRON,¹ STEVEN L. FINKELSTEIN,¹ OSCAR A. CHAVEZ ORTIZ,¹ DUSTIN DAVIS,¹ ERIN MENTUCH COOPER,^{1,2}
3 INTAE JUNG,^{3,4} DELANEY R. WHITE,¹ GENE C. K. LEUNG,¹ KARL GEBHARDT,¹ VIVIANA ACQUAVIVA,^{5,6}
4 WILLIAM P. BOWMAN,^{7,8} ROBIN CIARDULLO,^{7,8} ERIC GAWISER,⁹ CARYL GRONWALL,^{7,8} GARY J. HILL,^{2,1}
5 WOLFRAM KOLLATSCHNY,¹⁰ MARTIN LANDRIAU,¹¹ CHENXU LIU,¹ DANIEL N. MOCK,¹² AND ARIEL G. SÁNCHEZ¹³

6 ¹Department of Astronomy, The University of Texas at Austin, 2515 Speedway, Austin, TX 78712, USA

7 ²McDonald Observatory, University of Texas at Austin, 2515 Speedway, Austin, TX 78712, USA

8 ³Astrophysics Science Division, NASA Goddard Space Flight Center, Greenbelt, MD 20771, USA

9 ⁴Department of Physics, The Catholic University of America, Washington, DC 20064, USA

10 ⁵Physics Department, NYC College of Technology, 300 Jay Street, Brooklyn, NY 11201, USA

11 ⁶Center for Computational Astrophysics, Flatiron Institute, New York, NY 10010, USA

12 ⁷Department of Astronomy & Astrophysics, The Pennsylvania State University, University Park, PA 16802, USA

13 ⁸Institute for Gravitation and the Cosmos, The Pennsylvania State University, University Park, PA 16802, USA

14 ⁹Department of Physics and Astronomy, Rutgers, The State University, Piscataway, NJ 08854, USA

15 ¹⁰Institut für Astrophysik, Universität Göttingen, Friedrich-Hund Platz 1, D-37077 Göttingen, Germany

16 ¹¹Lawrence Berkeley National Laboratory, 1 Cyclotron Road, Berkeley, CA 94720, USA

17 ¹²Department of Physics, Florida State University, Tallahassee, Florida 32306

18 ¹³Max-Planck-Institut für extraterrestrische Physik, Postfach 1312, Giessenbachstr., 85748 Garching, Germany

ABSTRACT

We present the results of a stellar-population analysis of 72 Ly α emitting galaxies (LAEs) in GOODS-N at $1.9 < z < 3.5$ spectroscopically identified by the Hobby-Eberly Telescope Dark Energy Experiment (HETDEX). We provide a method for connecting emission-line detections from the blind spectroscopic survey to imaging counterparts, a crucial tool needed as HETDEX builds a massive database of ~ 1 million Ly α detections. Using photometric data spanning as many as 11 filters covering $0.4 < \lambda (\mu\text{m}) < 4.5$ from the *Hubble* and *Spitzer* Space Telescopes, we study the objects' global properties and explore which properties impact the strength of Ly α emission. We measure a median stellar mass of $0.8_{-0.5}^{+2.9} \times 10^9 \text{ M}_\odot$ and conclude that the physical properties of HETDEX spectroscopically-selected LAEs are comparable to LAEs selected by previous deep narrow band studies. We find that stellar mass and star formation rate correlate strongly with the Ly α equivalent width. We then use a known sample of $z > 7$ LAEs to perform a proto-study of predicting Ly α emission from galaxies in the Epoch of Reionization, finding good agreement between prediction and observation for the majority of strong emitters.

1. INTRODUCTION

Lyman-alpha emitting galaxies (hereafter LAEs) have fascinated astronomers for decades, from when Partridge & Peebles (1967) first predicted that primitive galaxies in formation could emit a detectable Ly α line, through their discovery by Cowie & Hu (1998) and Rhoads et al. (2000). These objects exhibit strong emission of the Ly α photon corresponding to the $n = 2$ to $n = 1$ resonant transition in hydrogen atoms. These photons are expected to face high optical depths from

neutral hydrogen to escape the galaxies in which they are generated, and dust grains along their paths can absorb them. To date, despite enormous effort (see Ouchi et al. 2020 for review), the community has not formed a strong consensus on exactly how Ly α radiation escapes its host galaxy, and no reliable model exists to predict the Ly α luminosity or equivalent width, $W_\lambda(\text{Ly}\alpha)$, of a galaxy given its global physical properties, such as stellar mass, metallicity, age, star formation rate, and dust extinction.

Part of the problem arises from discrepant conclusions drawn from studying LAEs identified using different selection techniques. Locally ($z \ll 1$), the ultraviolet

(UV) flux measured in wide or narrow-band filters often defines LAE samples, biasing studies to brighter, higher mass systems than those found spectroscopically (Hayes et al. 2014). Observations in the nearby universe paint LAEs as low mass galaxies with young stellar ages as determined from spectral energy distribution (SED) fitting, and many studies concur on trends showing an increase in Ly α luminosity with decreasing dust and metals (Hayes 2015). Nonetheless, many galaxies show stronger Ly α emission than models would predict based on dust extinction (e.g., Martin et al. 2015, Atek et al. 2014, Scarlata et al. 2009, Finkelstein et al. 2009), and a satisfactory explanation of this Ly α enhancement does not currently exist.

With narrow-band selected LAEs at higher redshift, discrepant results still persist. Finkelstein et al. (2009) found LAEs at $z \sim 4.5$ represent a diverse population in terms of stellar age, mass, and dust extinction. Finkelstein et al. (2015) modeled the SEDs of IRAC-detected LAEs at $z \sim 5$ and found a third have old stellar populations, contrasting with the young populations found in the local universe, and Guaita et al. (2011) observed similar heterogeneous populations in a narrow-band selected sample at $z \simeq 2.1$. Moreover, Gawiser et al. (2007) found NB-selected LAEs at $z = 3.1$ to generally be low mass, dust-free objects, but their model allowed for both young and more evolved stellar populations. Studies of LAE samples compiled using detection of the Ly α emission line itself in the high-redshift universe confound consensus as well. Hagen et al. (2016) used the Hobby Eberly Telescope Dark Energy Experiment (HETDEX) pilot survey (Adams et al. 2011, Blanc et al. 2011) to compare properties of LAEs at $z \sim 2$ with optical emission line-selected galaxies (oELGs) and found no significant differences between the populations. Remarkably, even the UV-slope did not differ in the two samples, implying either that diffuse dust in the interstellar medium (ISM) did not modulate Ly α emission or that oELGs strongly emit Ly α . Recently, spectroscopic surveys have also yielded confusing results about LAEs at $z > 2$. Using data from the VANDELS survey, Marchi et al. (2019) suggested LAEs have low mass and low dust extinction, but found no correlation with star formation rate. From the VIMOS Ultra-Deep Survey, Hathi et al. (2016) concurred with LAEs having lower mass and lower dust extinction, but they found that the objects have lower SFRs than non-LAEs.

A deeper understanding of what makes LAEs unique from other star forming galaxies (SFGs) tantalizes astrophysicists because of the profound implications for leveraging LAEs as sensitive probes of reionization at late $z \gtrsim 6$. Whether the Universe re-ionized rapidly at late

times (e.g. Robertson et al. 2015) or gradually beginning very early in its history (e.g. Finkelstein et al. 2019) can determine if massive, rare galaxies or low-mass, ubiquitous objects emitted the needed ionizing photons. Answering such a fundamental cosmological question hinges on our ability to detect neutral hydrogen in the Universe's infancy. Crucially, the attenuation of Ly α photons can probe the presence of neutral hydrogen in the intergalactic medium (IGM) (e.g, Miralda-Escudé 1998; Malhotra & Rhoads 2004; Dijkstra 2014), but the photons also undergo complicated resonant scattering within the galaxy, complicating our understanding of how much of the emission exits the ISM and circumgalactic medium (CGM) and enters the IGM in the first place. Recent attempts to use Ly α as a reionization probe have struggled to account for the intrinsic effects of host galaxy properties on the Ly α luminosity before the radiation encounters the IGM, leaving an unknown systematic uncertainty present in their results. The most detailed spectroscopic studies of post-reionization LAEs point to the covering fraction of optically thick neutral hydrogen (e.g. Reddy et al. 2021) as the key predictor of Ly α escape, but such observations remain expensive and time intensive. Finding correlations between Ly α emission and global properties such as mass and star formation activity, which photometry can reliably measure even at very high redshifts, could be a path forward to predicting galaxies' intrinsic Ly α output.

Small LAE sample sizes (< 20) were typical a decade ago, and samples of < 100 objects are still the norm. This has statistically hindered the efficacy of studies of global property correlations with Ly α emission. The HETDEX project (Hill et al. 2008, Hill et al. 2021, Gebhardt et al. 2021) is in the process of discovering a transformative sample of LAEs, clearing the way for the community to obtain a better understanding of this intriguing population. The un-targeted (targets not pre-selected), spectroscopically selected HETDEX LAE sample at $1.9 < z < 3.5$ provides a unique vantage point of galaxy evolution, as these galaxies probe the lower-mass end of the galaxy distribution, making them analogous to typical galaxies discovered in the epoch of reionization (e.g., Finkelstein et al. 2010).

As the first step toward realizing HETDEX's ability to unlock LAEs as probes of reionization, we present an initial study detailing how to link detections from the survey to imaging counterparts, and we provide an SED fitting analysis of their stellar population properties. Our modest sample of 72 LAEs in the GOODS-N field will pave the way for future large samples from HETDEX to obtain the best understanding of LAEs to

date. In §2 we describe how we built our sample and selected imaging counterparts. In §3 we describe our SED fitting procedure. We present our results in §4, comparing them to other studies, and we discuss our interpretations in §5. Finally, we attempt to predict the Ly α emission from a sample of epoch of reionization (EoR) galaxies in §6 and summarize this study in §7. In our analysis, we adopt a flat Λ CDM cosmology with $H_0 = 70 \text{ km s}^{-1} \text{ Mpc}^{-1}$ and $\Omega_m = 0.30$.

2. METHODOLOGY

In order to explore how Ly α emission from galaxies depends on stellar population properties, we built a sample of LAEs using emission line detections from the HETDEX survey, carefully identifying them as Ly α or other contaminant features, such as [O II] $\lambda\lambda 3726, 3729$, which is unresolved at HETDEX resolution. We then created a procedure for assigning the line detections to imaging counterparts in *HST* data so that we could proceed with fitting their SEDs.

2.1. The HETDEX Survey

With HETDEX the upgraded Hobby-Eberly Telescope (Ramsey et al. 1994, Hill et al. 2021) is observing an area of 540 deg^2 in the north Galactic cap and on the celestial equator using up to 78 pairs of integral-field spectrographs that span $350 - 550 \text{ nm}$ at $R \sim 800$. Each spectrograph pair is fed by an integral field unit (IFU) of 448 $1.5''$ -diameter fibers which cover a $51'' \times 51''$ region on the sky with $1/3$ fill factor (Kelz et al. 2014; Hill et al. 2021). Each HETDEX observation consists of three 6-min dithered exposures to fill in the area between fibers, each with $>30,000$ individual fibers. The majority of these fibers just contain blank sky, but some subset contain continuum sources such as stars or emission lines from both nearby and distant galaxies.

Gebhardt et al. (2021) describe the data reduction and calibrations needed to convert the raw observations into a three dimensional spectroscopic data set as well as the methods used to detect emission lines contained in the millions of observed spectra. As a brief summary, HETDEX reductions involve three types of calibration frames: biases (taken nightly), pixel flats (taken yearly using a laser-driven light source), and twilight sky flats (taken nightly and averaged monthly), which are used for bias subtraction, bad pixel masking, fiber profile tracing, wavelength calibration, scattered light removal, spectral extraction, fiber normalization, spectral masking, and sky subtraction. These frames, combined with sky background on science images, produce a wavelength calibrated, sky-subtracted spectrum for each fiber in the array.

Astrometric calibrations are achieved by measuring the centroid of each field star and comparing their positions on the IFUs to the stars' equatorial coordinates in the Sloan Digital Sky Survey (SDSS; York et al. 2000; Abazajian et al. 2009) and *Gaia* (Gaia Collaboration et al. 2018) catalogs. This process typically results in global solutions which are good to $\sim 0.2''$ and no worse than $\sim 0.5''$, with the exact precision of a measurement dependent upon the number of IFUs in operation at the time of the observation.

To find emission lines, the data pipeline searched every spatial and spectral resolution element in the internal HETDEX data release 2 (HDR2) to look for a peak in signal. Regions of enhanced signal were fit with a single Gaussian model. The exact location was determined by rastering on a grid and maximizing the line's signal-to-noise (S/N). An internal catalog of high-quality emission lines was generated by Cooper et al. (in preparation), and we drew our initial sample from the HDR2 version of that catalog. The catalog reduced the raw detected line emission sources as described in Gebhardt et al. (2021) into a more robust sample by passing the observations through a quality assessment pipeline and limiting various fitted line parameters. Specifically, emission lines were required to have a quality of fit, $\chi^2 < 1.2$ and a linewidth, σ , in the Gaussian model between 1.7 \AA and 8 \AA . The full HETDEX survey will eventually detect ~ 1 million LAEs, providing an incredible opportunity to study such objects, but our analysis is focused on LAEs discovered in 2018–2020 data from a HETDEX science verification field in GOODS-N, a roughly $10' \times 16'$ field centered at (J2000) $12^{\text{h}}36^{\text{m}}55^{\text{s}}$, $62^{\circ}14^{\text{m}}15^{\text{s}}$ (Giavalisco et al. 2004, Grogin et al. 2011, Koekemoer et al. 2011) because we required deep, multi-band imaging to study each galaxy's stellar populations.

2.2. Sample Selection

We visually inspected HETDEX detections in GOODS-N to obtain a clean sample of LAEs. To get initial candidates, we applied various quality cuts to the curated catalog for data release HDR 2.1.2 (Cooper et al., in preparation). We restricted emission line detections to those with signal-to-noise ratio $S/N > 5.5$ to limit the fraction of spurious detections from noise fluctuations to less than 5% (see Gebhardt et al. 2021) as well as $\chi^2 < 1.6$ for the Gaussian model fit, which was a value tuned to remove the most obvious artifacts while retaining the largest sample for inspection. We required emission line full-width at half-maximum (FWHM) between 3.4 \AA and 24 \AA , where the lower bound removed exceedingly narrow peaks arising from unidentified cosmic rays and the upper bound removed emission gener-

ated by broad-line AGNs, which we considered contaminants in this study (see §3.1). We further only included observations with throughput > 0.07 for reliable flux measurements minimally affected by cloud cover, and seeing below $2.8''$ to enable continuum counterpart identification. We did not remove “repeat” detections coincident spatially and spectrally resulting from the survey revisiting the field multiple times in order to ensure we found as many Ly α detections as possible. We excluded data in GOODS-N taken prior to 2018 as they included significant artifacts from early CCDs that had been replaced by 2018.

Finally, we did not initially remove any detections based on the Bayesian probability values used to help determine the identity of an emission line as Ly α vs [O II] $\lambda\lambda 3726, 3729$. These probabilities, which are calculated by the HETDEX team based on the work of Leung et al. (2017) and Farrow et al. (2021), leverage the inherent differences between the emission line luminosity and equivalent width (EW), W_λ , distribution functions of LAEs and [O II] emitters to identify single emission line detections using information about the line flux and continuum emission, when available. During the process of visual inspection, we used the statistic to guide our identifications, and we make recommendations for using quality cuts based off this statistic at the end of this section.

After applying quality cuts, we began with 842 detections (of which ~ 500 were “unique” in the sense that there were no other emission line detections within $3''$ spatially and 6 \AA spectrally). To inspect each detection, we used the HETDEX Emission Line eXplorer tool ELiXer (Davis et al., in preparation), which shows measured quantities for the emission lines such as S/N , line width, line fit χ^2 , the continuum estimate, the Bayesian probability for Ly α emission described above, as well as useful visual information, such as cutouts of the 2D spectra for several fibers containing the feature, the Gaussian model fit to the feature, the full 1D spectrum, and any imaging and catalog data uploaded in the HETDEX pipeline.

We rated our confidence in a detection on a scale of 0–5 using a customized widget tool that allows interactive classification of detected sources based on the its Elixer Report (see Figure 1). Additionally, other classifications include “artifact,” a false detection caused by a malfunction in the instrument or the reduction pipeline, low-redshift sources, and “other” for miscellaneous objects like meteors. To qualify for a classification of 4 or 5 (a high-confidence LAE by our definition), a detection had to meet the following criteria:

- A clear emission line in at least one fiber in the un-smoothed 2D spectrum, or a probable emission line in at least two fibers. Since each point-spread-function (PSF) covers multiple fibers (due to the dithering pattern), we expected strong emission to be seen in more than one fiber, increasing the likelihood of a real detection.
- No obvious defects at the emission line location in the pixel flat or sky subtraction cutouts. This eliminated hot pixels, sky model residuals, charge traps, and other artifacts from the sample.
- A Gaussian model fit that adequately matched the data and did not have a FWHM far below the spectral resolution of $\sim 6 \text{ \AA}$.
- A line peak that exceeded the typical noise level in multiple pixels in the 1D spectrum.
- No source at the line’s detection position brighter than roughly $m_{AB} = 24$ in the imaging cutouts, if available. The high equivalent widths of sources fainter than this threshold drastically decrease the likelihood of contamination by [O II] emitters (see Figure 6 in Leung et al. 2017), though a few low equivalent width, luminous LAEs can be missed with this requirement.

As the [O II] $\lambda\lambda 3726, 3729$ emission feature falls into the $3500 \text{ \AA} < \lambda < 5500 \text{ \AA}$ spectral range for $z < 0.5$, the imaging proved crucial in choosing between high-redshift LAEs and interloping [O II] emitting galaxies.

Figure 1 shows an example ELiXer report for a source classified as a high-redshift LAE. A clear emission feature is present as a black signal in three out of the four 2D un-smoothed fiber spectra, the sky subtraction looks clean, the model fit accurately represents the data, and the image stamps show a number of faint sources with photometric redshift estimates reasonably close to the Ly α redshift (shown by the vertical red dashed line). Figure 2 shows a clear example of a low-redshift object detected by its [O II] emission line. As in Figure 1, the line appears strong in multiple fibers, and the sky subtraction and model fit present no concerns. Characteristically of a brighter low-redshift galaxy, continuum emission is visible as a horizontal black trace in the fiber spectra, and a large, bright object appears in the *HST* image stamps. In this case, the object is in fact a catalogued [O II] emitter, but even without such information this would be a clear low-redshift classification. In both of these cases, no other emission lines are detected, or would be expected to be detectable, across the observed wavelength range.

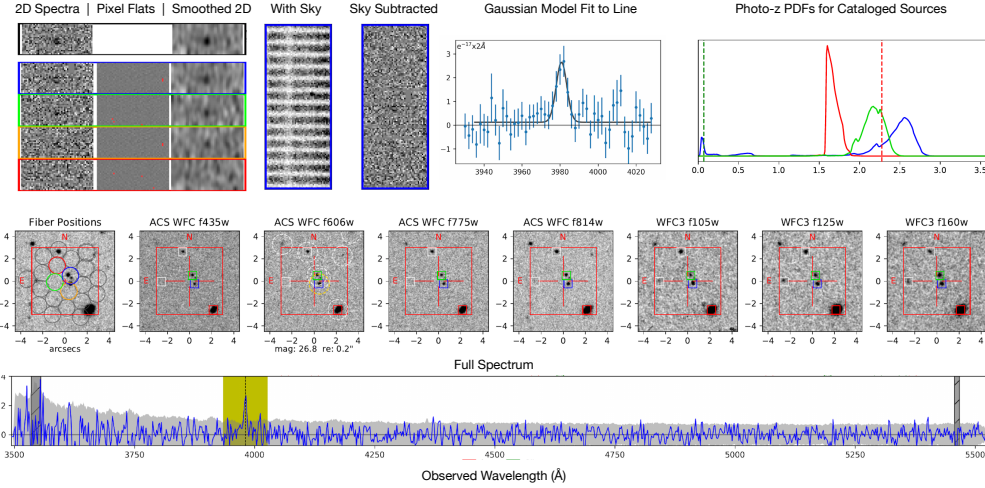


Figure 1. A section of an ELiXer report for detection ID 2100325857, corresponding to an LAE in our sample. The report contains information about the detected line as well as any available imaging at the detection position (see section 2.3) used to classify the line. In the top left corner, outlined by colorful rectangles, are the 2D spectra from the four fibers contributing the highest S/N to the detection; the stacked signal is shown on the top row, outlined in black. The pixel flats and smoothed 2D spectra are displayed in the right two columns. Moving to the right, the report shows the sky subtraction quality and the Gaussian model line fit to the emission and continuum level (black line). The middle row contains $10''$ imaging cutouts with the fiber positions shown in gray in the first image and the locations of cataloged sources marked with colorful boxes in all subsequent images. The AB magnitude of the nearest likely source is also reported (in this case 26.8). The top right corner shows the photometric redshift probability distributions calculated by the CANDELS team (B. Andrews et al., in preparation) for sources of the same color in the imaging. In this plot, the redshifts assuming [O II] and Ly α are shown as vertical dashed green and red lines, respectively. Finally, the bottom row shows the full 1D spectrum, allowing the inspector to assess the overall noise fluctuations and the continuum level.

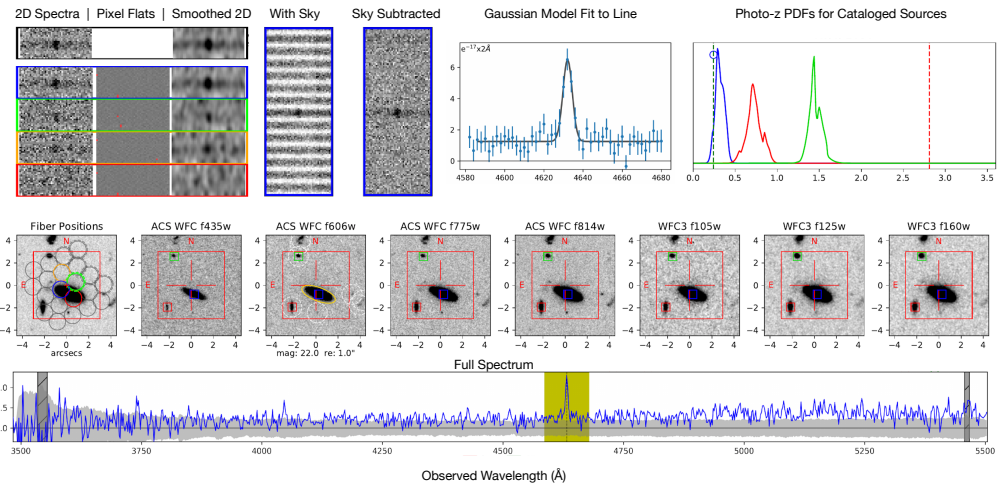


Figure 2. A section of an ELiXer report, in the same format as Figure 1, for detection ID 2100037191, corresponding to the [O II] $\lambda\lambda$ 3726, 3729 feature in a galaxy at $z \approx 0.24$. The black trace in the 2D fiber spectrum (blue rectangle) indicates a clear detection of continuum emission, which is also evident in the 1D spectrum in at the bottom of the figure. The imaging shows a large, bright source ($m_{AB} = 22.0$) centered on the detection position, and the source has a cataloged spectroscopic redshift consistent with [O II] indicated as an open blue circle in the upper-right corner.

After classifying each detection, we obtained ~ 200 detections categorized as high confidence LAEs (scores of 4-5) and almost three times as many classified as low- z sources (Figure 3). Note that we did not include detections with scores of 3 or below for initial study as we want the cleanest sample possible. To assess the HETDEX collaboration's built-in Bayesian classification probability, $P(\text{Ly}\alpha)$, we plotted that statistic for all of our detections classified as either low- z galaxies or LAEs. Figure 4 shows that true LAE detections rarely score low in the $P(\text{Ly}\alpha)$ statistic, but a few low- z sources can score in the intermediate range. For this reason, we suggest future studies can dramatically reduce the amount of visual inspections needed by adopting a cut-off of $P(\text{Ly}\alpha) \gtrsim 0.6$ for LAE candidates.

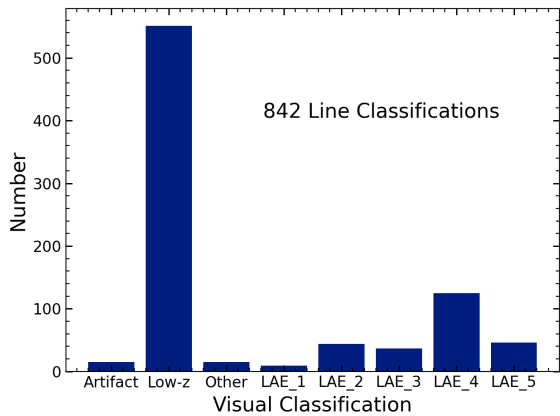


Figure 3. The distribution of visual classifications of candidate detections. Making cuts based on $P(\text{Ly}\alpha)$ to remove low- z sources can dramatically reduce the visual inspection workload.

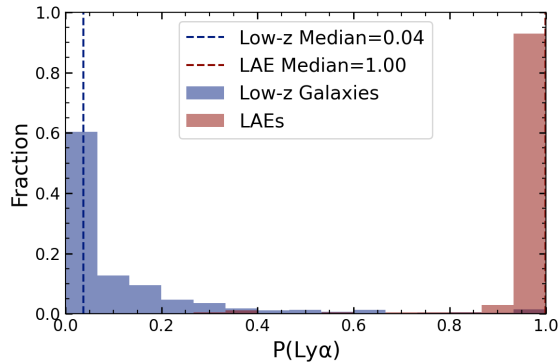


Figure 4. The distribution of $P(\text{Ly}\alpha)$ for detections visually classified as low-redshift galaxies (light blue) and high-confidence (scores of 4 and 5) LAEs (light red). Adopting a minimum threshold for $P(\text{Ly}\alpha)$ can remove a large fraction of low-redshift interlopers without eliminating very many LAEs.

To finalize our sample, we removed detections of the same source (since the GOODS-N field was observed multiple times between 2018–2020), by selecting the highest S/N measurement of all detections grouped within $2''$ and one spectral resolution element (6 \AA). Our final emission line sample consisted of 94 high-confidence Ly α detections (with classification scores of 4-5).

2.3. Counterpart Identification

In order to study the stellar populations of the LAEs in our sample, we developed a method to match the un-targeted spectroscopic detections to counterparts in *HST* imaging of the GOODS-N field.

The overall astrometric precision of a HETDEX observation is $\sim 0.2''$. However, due to the $1.5''$ diameters of the fibers, the typical seeing, and the 3-dither pattern, the position of an individual (faint) LAE is known to no better than $\sim 0.5''$. Since the HST images have a resolution that is ~ 20 times higher than this, great care is needed to ensure an emission-line source is matched with the correct counterpart.

We used the imaging obtained by the Great Observatories Origins Deep Survey (GOODS [Giavalisco et al. 2004](#)) with the optical ACS camera, and the Cosmic Assembly Near-infrared Deep Extragalactic Legacy Survey (CANDELS [Grogin et al. 2011; Koekemoer et al. 2011](#)) with the WFC3/IR infrared camera, using the internal CANDELS team's reduced mosaics for each filter. This dataset consists of imaging in nine filters (F435W, F606W, F775W, F814W, F850LP with ACS, and F105W, F125W, F140W and F160W with WFC3/IR). We made use of the photometric catalogs derived by [Finkelstein et al. \(2021\)](#) which used SOURCE-EXTRACTOR ([Bertin & Arnouts 1996](#)) in two-image mode to create a F160W-selected catalog, coupled with using the Tractor ([Lang et al. 2016](#)) to perform de-blended photometry on the deep S-CANDELS ([Ashby et al. 2015](#)) *Spitzer*/IRAC 3.6 and $4.5 \mu\text{m}$ imaging. Further details on the cataloguing process are available in [Finkelstein et al. \(2021\)](#). Similar to the widget used to classify detections as Ly α , we created a visual inspection tool that provided information about the distance between the centroid of the HETDEX emission location and a given imaging source, the HETDEX emission line strength when re-extracted centered at the imaging counterpart position, and the goodness of an SED fit assuming the Ly α redshift, $z_{\text{Ly}\alpha}$.

Before selecting counterpart candidates, we optimized our search by developing a deep photometric catalog using a stacked image across all *HST* filters in GOODS-N. Each pixel value in this image and its error was computed using an inverse variance weighted average across

⁴²⁷ $N = 9$ filters with pixel value p_i and rms error σ_i given
⁴²⁸ by Equation 1.

$$\bar{p} = \frac{\sum_i^N p_i \sigma_i^{-2}}{\sum_i^N \sigma_i^{-2}}, \quad \sigma_{\bar{p}} = \left(\sum_i^N \sigma_i^{-2} \right)^{-1/2} \quad (1)$$

⁴³⁰ Since LAEs are often low-mass, faint systems, this
⁴³¹ stacked image improved our chances of identifying the
⁴³² continuum source corresponding to the detected emis-
⁴³³ sion line.

⁴³⁴ We then used SOURCEEXTRACTOR (Bertin & Arnouts
⁴³⁵ 1996) to detect the faintest possible sources in the
⁴³⁶ stacked image, requiring a source to have 5 contiguous
⁴³⁷ pixels with $S/N > 1.6$. Following the procedures out-
⁴³⁸ lined in Finkelstein et al. (2021) we used the same soft-
⁴³⁹ ware in two-image mode to measure the flux in each fil-
⁴⁴⁰ ter and applied the appropriate aperture correction ob-
⁴⁴¹ tained from simulations. We performed extinction cor-
⁴⁴² rections using a Cardelli extinction law with $R_V = 3.1$
⁴⁴³ for the Milky Way (Cardelli et al. 1989). We then com-
⁴⁴⁴ pared the fluxes measured in this catalog to the F160W-
⁴⁴⁵ selected catalog of Finkelstein et al. (2021) and found the
⁴⁴⁶ flux measurements to have no systematic offset and min-
⁴⁴⁷ imal scatter. Figure 5 shows the fractional error of the
⁴⁴⁸ stacked catalog photometry compared to the Finkelstein
⁴⁴⁹ et al. 2021 photometry as a function of source brightness
⁴⁵⁰ in the I -band. The median offset is zero with scatter of
⁴⁵¹ roughly 25% for fluxes near 100 nJy, in agreement with
⁴⁵² the typical error bars for such sources, providing confi-
⁴⁵³ dence in the fidelity of the stacked catalog. In all sub-
⁴⁵⁴ sequent analysis, we defaulted to using measurements
⁴⁵⁵ from the Finkelstein et al. (2021) catalog for sources de-
⁴⁵⁶ tected in both, and we only used photometry from the
⁴⁵⁷ stacked catalog for sources unique to it.

⁴⁵⁸ After generating the catalog from stacked imaging, we
⁴⁵⁹ identified all imaging sources within $3''$ of the HETDEX
⁴⁶⁰ detection position as possible LAE counterparts. Since
⁴⁶¹ the typical image quality of the HETDEX observations
⁴⁶² used here has a point spread function (PSF) of $\sim 1.7''$,
⁴⁶³ the $3''$ annulus served as a generous aperture around the
⁴⁶⁴ Ly α centroid to encompass all possible counterparts for
⁴⁶⁵ the detected emission.

⁴⁶⁶ We selected imaging counterparts based on the neigh-
⁴⁶⁷ boring sources' angular distances from the detection,
⁴⁶⁸ significance of emission extracted at the source posi-
⁴⁶⁹ tions, and goodness of SED fits performed by fixing
⁴⁷⁰ the redshift assuming a Ly α detection. First, we mea-
⁴⁷¹ sured the on-sky angular separation from the detection
⁴⁷² position to the position of each possible source in the
⁴⁷³ photometric catalog (labeled θ in Figure 6). Then,
⁴⁷⁴ for each source, we used the HETDEX API script,

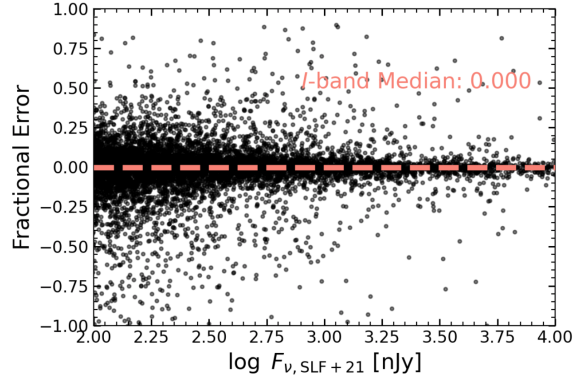


Figure 5. The fractional error between I -band (F775W) fluxes of sources measured in our derived stacked-detection catalog matched to sources in the original catalog from Finkelstein et al. (2021) as a function of flux in the latter catalog. The median offset is indicated with the dashed pink line, and its value is given with text, showing good agreement between these two catalogs.

⁴⁷⁵ `get_spectrum.py`¹, to perform an aperture-weighted
⁴⁷⁶ optimized spectral extraction (following Horne 1986) at
⁴⁷⁷ the source position to obtain a 1D spectrum. We cre-
⁴⁷⁸ ated a Markov chain Monte Carlo (MCMC) line-fitting
⁴⁷⁹ code using EMCEE (Foreman-Mackey et al. 2013) to fit
⁴⁸⁰ a model to the feature to estimate its flux and signifi-
⁴⁸¹ cance. Our model consisted of two components: a linear
⁴⁸² trend with slope m and intercept b , which captured any
⁴⁸³ underlying continuum, and a Gaussian with total flux F
⁴⁸⁴ and standard deviation σ to fit the line profile.

$$\text{⁴⁸⁵ } f_\lambda = m(\lambda - \lambda_0) + b + \frac{F}{\sqrt{2\pi}\sigma} \exp \left[-\frac{(\lambda - \lambda_0)^2}{2\sigma^2} \right] \quad (2)$$

⁴⁸⁶ In the model, λ_0 , the wavelength of the emission line,
⁴⁸⁷ was allowed to vary by \pm one pixel (2 \AA) from the detec-
⁴⁸⁸ tion wavelength reported by HETDEX. For each fit, we
⁴⁸⁹ measured an effective S/N ratio (labeled SNR in Fig-
⁴⁹⁰ ure 6) by comparing the median value of the line flux to
⁴⁹¹ the standard deviation of the line flux for the last 20%
⁴⁹² of the MCMC sampling chain, which had converged at
⁴⁹³ that stage of sampling. To limit computation time for
⁴⁹⁴ future counterpart identification steps, we ruled out any
⁴⁹⁵ counterpart candidates that did not have any indication
⁴⁹⁶ ($S/N > 1$) of an emission feature at the pixel corre-
⁴⁹⁷ sponding to the detected wavelength. Finally, for those
⁴⁹⁸ sources with significant emission, we performed SED fit-
⁴⁹⁹ ting with BAGPIPES (see Section 3.1 for a full description
⁵⁰⁰ of this procedure), fixing the redshift as $z_{\text{Ly}\alpha}$. Our sim-
⁵⁰¹ ple SED model for counterpart identification included

¹ https://github.com/HETDEX/hetdex_api

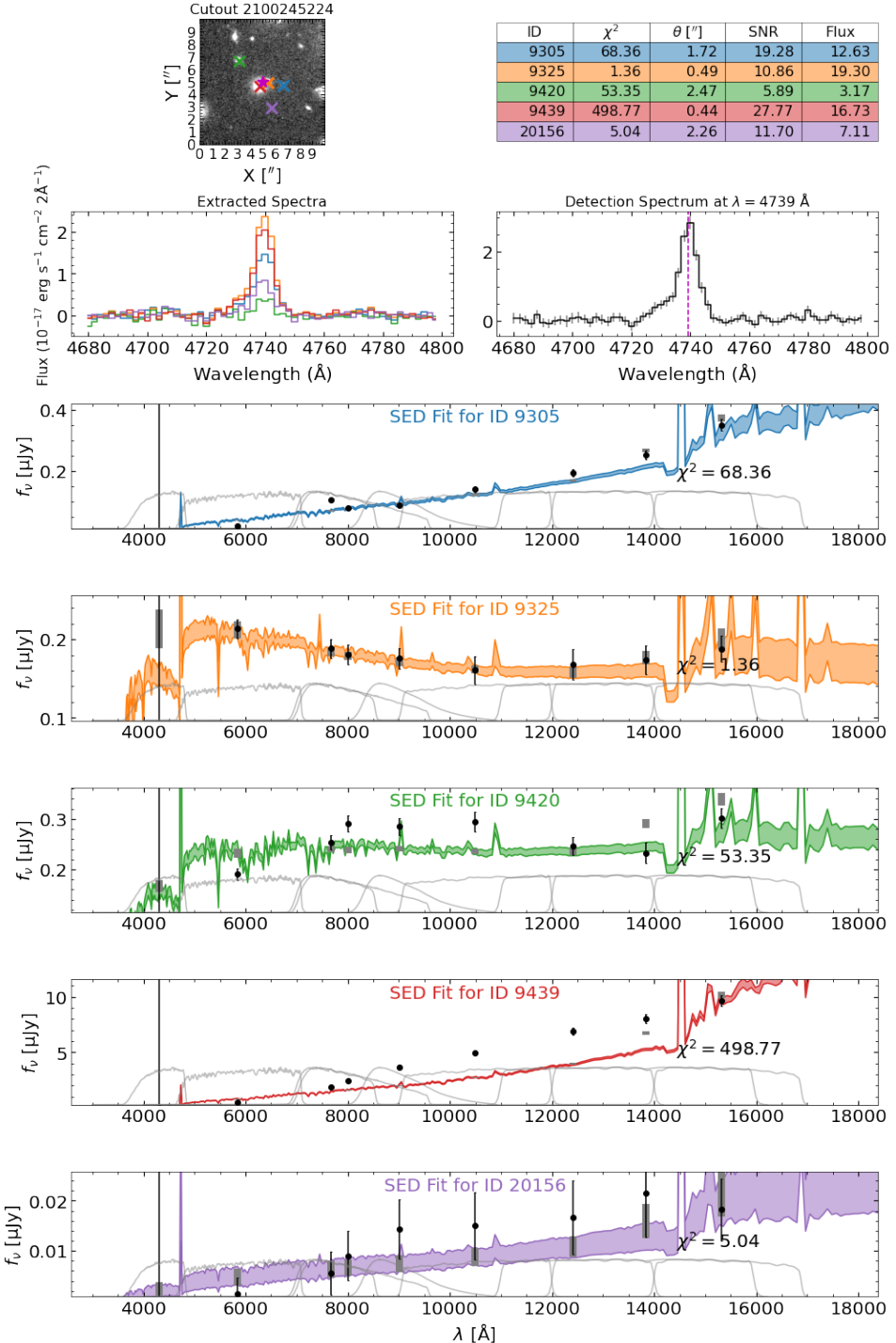


Figure 6. An example of the visualizations used to select imaging counterparts for Ly α detections. The figure shows a $10''$ image cutout with the detection positioned marked with a magenta star and sources marked with “X”’s of various colors, 1D spectra extracted at each source position, the original detection 1D spectrum, and SED fits (with redshift fixed assuming Ly α emission) of all sources with significant measured fluxes. The table in the top-right contains the χ^2 value of each SED fit, the separation between each source and the emission line detection position (labeled θ), and the significance (labeled SNR) and the line flux in $\text{erg s}^{-1} \text{cm}^{-2}$ of the emission line extracted at the source position. The colors are consistent across all plots and tables, so each source corresponds to a unique color. The SED plots also contain normalized filter response curves as gray lines. In this case, while the red and orange sources have similarly small distances from the detection position and similar line fluxes, the SED fit χ^2 strongly favors the orange source to be an LAE.

free parameters for stellar mass, metallicity, dust extinction, and SFH, and we adopted the Calzetti et al. (1994) dust attenuation law, the Chabrier (2003) initial mass function, and a delayed- τ SFH. At this stage, we did not include any IRAC fluxes in our fits since those fluxes depend sensitively on deblending, which is unreliable when sources are crowded. Furthermore, between $1.9 < z < 3.5$, there are no strong spectral features at the rest-frame wavelengths probed by IRAC, and redshift-sensitive features such as the 4000 Å break are adequately covered by *HST*. We then visually inspected the separations, spectral extractions, and SED fits of all candidate counterparts to choose the one most likely to be the detected LAE.

Figure 6 shows an example of our approach. Separate sources are marked with an “X” and the color of the mark corresponds to the color of the table row, spectrum, and SED in the subsequent plots. In this case, the red and orange sources within $0''.5$ of the detection position (magenta star) show similar extracted emission line flux at the detection wavelength. Crucially, the SED fit for the red object poorly matches the data when fixing the redshift as $z_{Ly\alpha}$, but the orange object has a fit in excellent agreement with its observed SED based on the χ^2 statistic. Therefore, in this example case we selected the orange object as the detected LAE. We followed the same process to identify counterparts for the other Ly α lines in our sample.

By studying the distribution of our counterparts in the parameter space of separation, signal-to-noise of emission, and SED χ^2 , we found no obvious way to select counterparts reliably based on these numbers alone, but we did find favorable regions. Figure 7a shows the distribution of separation from the detection positions for sources we identified as LAEs and sources that just happened to be nearby. Clearly, it was exceedingly unlikely that the true counterpart lay farther than $1''$ away on sky. For this reason, we could very reasonably shrink our selection criteria from all sources within $3''$ to roughly $1''$ without significant loss of LAEs. In terms of emission line S/N (compared to the measured value of the detection itself), we found that, while typically the identified counterparts had stronger emission, the HETDEX PSF caused the extracted flux to not depend sensitively enough on position to clearly identify the counterpart for sources separated by less than $1''$. This is clearest in Figure 8a, which shows that true counterparts and close neighbors show overlap in the S/N , separation plane. Note that the different on-sky centroids for emission line extraction between the counterparts and the original detection allow for the values of the S/N ratios in Figure 7b to be greater than unity. Finally, we note that, while

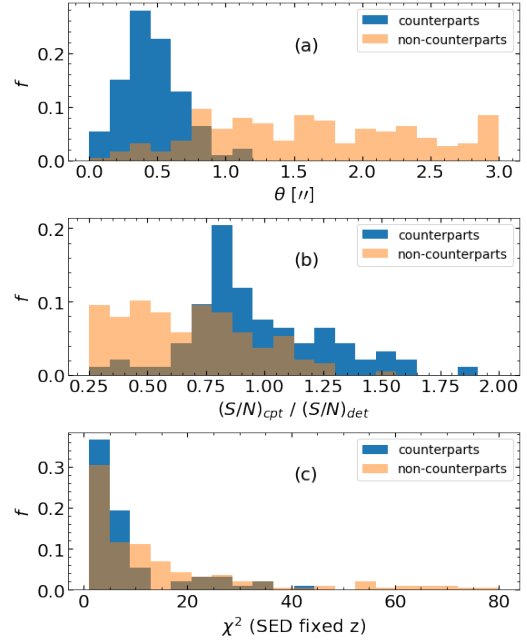


Figure 7. The distributions, expressed as the fraction of objects in a given bin, of (a) separation, (b) position-extracted emission line signal-to-noise (relative to that of the detection), and (c) SED χ^2 assuming $z_{Ly\alpha}$, for objects identified as the detection imaging counterparts and those that happened to be spatially coincident. Histograms are normalized to the population size. The top panel indicated that finding a counterpart with an imaging separation larger than $1''$ from the detection position is exceedingly rare.

most of the LAEs in our sample had χ^2 values in good agreement with the $z_{Ly\alpha}$ hypothesis, many neighboring galaxies also had low χ^2 , as shown in Figure 7c. We attribute the low χ^2 values for non-counterparts to our inclusion of such faint objects, which have large flux errors and are thus easily fit by a wide range of models.

After visually vetting all detections in our sample of 94 Ly α lines, we found 6 instances of detected emission with no continuum-detected counterpart. Since we could not study the properties of an LAE without photometry, we removed these objects from the final analysis. Furthermore, we removed 16 objects from the sample due to the following quality concerns. We eliminated the LAE corresponding to HETDEX detection ID 2100245124 (RA,DEC=189.346621°,62.260662°) from our sample as it was the only counterpart with an X-ray detection in the catalog of Xue et al. (2016), indicating the galaxy hosted an AGN. Since our SED fitting code did not have an AGN template, we could not reliably report the physical properties of this object. We also eliminated the detection for ID 2100171783, as the counterpart inspection revealed the Ly α emission line came from two probable LAEs separated by less than $0''.5$ meaning we could not

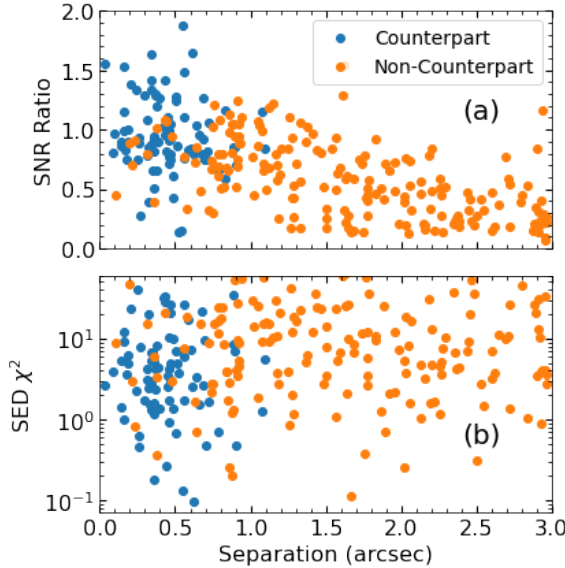


Figure 8. (a) The 2D distribution (in S/N and separation space) for objects identified as the imaging counterparts for emission line detections and those that happened to be spatially coincident. (b) The same plot in SED χ^2 and separation space. These two figures show substantial overlap in these parameter spaces for true LAEs and neighboring sources, motivating the benefits of detailed visual inspection shown in Figure 6.

assign flux accurately to each source. Finally, we only analyzed objects detected in the H -band (F160W) of the HST imaging as well as at least two bluer bands in order to span the rest-frame 4000 Å break at the sample redshift range. This serves as a crucial feature for constraining galaxy masses and ages with SED fitting (e.g., see Shapley et al. 2003). These choices limited our final sample size to 72 LAEs in GOODS-N spanning $1.98 < z < 3.48$. For 5 of these objects, photometry was not present in the catalog of Finkelstein et al. (2021), so we used photometry from the stacked catalog described in §2.3. Appendix B, Figure 20 shows all the HETDEX emission lines for the LAEs in the final sample, and Figure 21 shows HST imaging in F160W (H -band) for all objects.

3. ANALYSIS

After connecting HETDEX emission line detections with HST imaging counterparts, we leveraged SED fitting to measure the galaxies’ stellar population properties. From the SED fits and emission line detections, we also inferred the UV-slope and Ly α equivalent width.

3.1. SED Fitting with BAGPIPES

We fit all LAEs in our final sample with BAGPIPES (Carnall et al. 2018), a flexible PYTHON code that

rapidly generates galaxy model spectra through stellar population synthesis using the 2016 version of the Bruzual & Charlot (2003) stellar spectral libraries. It explores the high-dimensional, multi-modal, and degenerate (e.g., age-dust-metallicity) model parameter space using the MULTINEST algorithm (Feroz & Skilling 2013).

Our sample in GOODS-N had photometry across nine HST filters ranging from 0.4 to 1.6 μm as well as two $Spitzer$ /IRAC channels centered at 3.6 μm and 4.5 μm . Translating to the rest-frames of the objects in our sample at $1.9 < z < 3.5$, these filters probed the UV, optical, and near-infrared (NIR) energy output of our objects.

The filter coverage of our sample of LAEs motivated our choice of SED modeling parameters. Table 1 shows the names and units of the free parameters in our model, as well as the prior probability distributions assumed in our Bayesian framework. We adopted a delayed- τ SFH, defined as:

$$\text{SFR}(t) \propto \begin{cases} (t - t_0)e^{-(t-t_0)/\tau} & t > t_0 \\ 0 & t < t_0 \end{cases} \quad (3)$$

This flexible SFH allows for star formation to be either rising, peaking, or falling, as opposed to the common exponentially declining model that only allows for falling SFRs over time. For example, Lee et al. (2010) found that SED fitting that adopted rising SFHs matched the stellar masses and SFRs from semi-analytic models for galaxies at $3 < z < 6$ better than exponentially declining models, while Papovich et al. (2011) found similar results favoring rising SFHs for real galaxies at $z = 4$ –7. We fit the e -folding scale of the SFH, τ , the age of the Universe at the onset of star formation, t_0 , the stellar mass formed, M_{form} , the global metallicity, Z , the dust extinction in the V -band, A_V , and the ionization parameter, $\log U$, defined as the log of the ratio of the number densities of ionizing photons and hydrogen atoms. We note that some of these parameters (namely Z and U) are not expected to be well-constrained by our photometric data. Nonetheless we allow them to vary within our imposed priors such that the uncertainties in the other parameters include the uncertainties in these parameters. We adopted the Calzetti et al. (1994) dust attenuation law for star-forming galaxies and the Chabrier (2003) initial mass function.

All 11 filters were not necessarily included for every galaxy SED fit in our sample. For example, due to the large PSF of the IRAC imager, modeling sources in crowded fields of view and deblending the flux contribution of each source is crucial to accurately measuring the NIR fluxes of our LAEs. Although the catalog we used performed deblended photometric modeling with

Parameter	Prior	Bounds	Units
t_0	Uniform	$0, T(z)$	Gyr
τ	Uniform	0.3, 10.	Gyr
M_{form}	Log Uniform	$10^6, 10^{12}$	M_\odot
Z	Log Uniform	$10^{-5}, 2$	Z_\odot
A_V	Uniform	0, 2	mag
$\log U$	Uniform	-4, -2	-

Table 1. Free parameters and their prior probability distributions for SED fitting. In our galaxy models, the redshift, z , was fixed based on the observed wavelength of Ly α from HETDEX. $T(z)$ refers to the age of the Universe at redshift z . Note that we fit the cumulative stellar mass formed, M_{form} , from which the stellar mass at the object redshift was computed within the BAGPIPES (Carnall et al. 2018) code

the IRAC PSF, this process can fail in crowded regions. We thus visually inspected all IRAC residual maps for objects in our sample and removed the IRAC fluxes from our SED fitting if there were obvious problems in the deblending procedure. For the 5 objects not present in the catalog of Finkelstein et al. (2021), we did not have IRAC measurements. Furthermore, because the purpose of our analysis was to study the SED-derived properties of our LAEs in relation to their Ly α emission, we did not want BAGPIPES’s modeling of Ly α emission or the IGM attenuation to bias our results. For this reason, we masked out all filters whose bandpass extended blue-ward of the observed Ly α line; thus the B -band (F435W) and sometimes the V -band (F606W) was excluded, depending on redshift.

Figure 9 shows an example BAGPIPES SED fit for an LAE in our sample. We plotted the 1σ spread on the model photometry as rectangles as well as the 1σ spread on the underlying model spectrum computed by evaluating the 16th and 84th percentiles of the posterior models. In this example, the fit did an excellent job matching salient features like the rest-frame 4000 Å break and nebular emission in the rest-frame optical region. We estimated galaxy properties using the posterior distributions for all free parameters explored by BAGPIPES. Figure 10 shows an example “corner” plot (produced via Foreman-Mackey 2016), where all free parameters are plotted against each other for easy assessment of constraints and correlations. Stellar mass, time since the onset of star formation, and dust extinction were constrained well, while metallicity, τ , and ionization parameter were not well-constrained by our broadband photometry data. Figure 19 in Appendix B shows the SED fits for all 72 LAEs in our final sample.

3.2. Measuring $W_\lambda(\text{Ly}\alpha)$ and β

Emission line strengths can be represented by the parameter equivalent width (EW or W_λ), which represents the width of a rectangle drawn to the same height as the continuum needed for the rectangular area to match the area under the emission line. To estimate the equivalent width of HETDEX Ly α detections, we used the measured line flux and error from the internal HDR 2.1.3 catalog computed by optimally extracting flux from all fibers within a 3.5 " radius circular aperture (roughly 15-20 individual fiber spectra) contributing to the emission line detection (following Horne 1986), weighted by the PSF of a point-source. We approximated the continuum flux density using the BAGPIPES sampled model spectra from the SED fit. We took the continuum flux density to be the median value of all 500 sampled spectra averaged between 1250 and 1300 Å in the given object’s rest-frame, and we computed the 1σ error using half the spread between the 16th and 84th percentiles of those values. This method allowed us to take advantage of complex computations performed by BAGPIPES to get a statistically representative estimate of the continuum flux density instead of using a coarse approximation based off the flux in one of our photometric bands. We evaluated the Ly α flux and the continuum flux density in the observer-frame and translated to the galaxy rest-frame by dividing by a factor of $(1+z)$ using the detected wavelength of Ly α .

$$W_\lambda(\text{Ly}\alpha) = \frac{F_{\text{Ly}\alpha}}{f_\lambda} (1+z)^{-1} \quad (4)$$

We measured β , the UV continuum slope (uncorrected for dust), using the model spectra for galaxies in our sample following the method described in Finkelstein et al. (2012). We masked the stellar and interstellar absorption features in the rest-frame UV using the windows provided by Calzetti et al. (1994), and we fit a linear model to the spectrum in log space ($\log f_\lambda = \beta \log \lambda + C$) using *polyfit* from the PYTHON package NUMPY (Harris et al. 2020). We determined 1σ uncertainties on β for each object by measuring the distribution of values fitted to 500 spectral models sampled from the posterior by BAGPIPES.

4. RESULTS

We measured various physical properties of objects in our LAE sample using the posterior distributions returned by BAGPIPES’ exploration of the parameter space. We took the 16th and 84th percentiles of the posterior distributions to represent the error bars on physical properties. Examples of such measurements are shown in Figure 10 for a representative LAE in our sample.

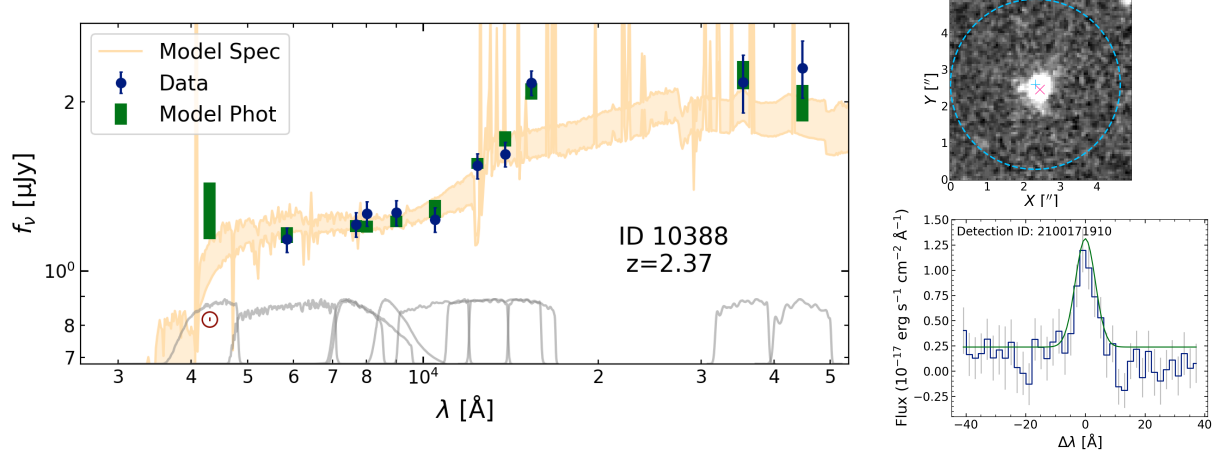


Figure 9. (Left): An example fit to the SED of an LAE in the sample. Data are shown by blue circles, and the 68% spread for the posterior model photometry and spectrum are shown by the green rectangles and orange shaded lines, respectively. A maroon open circle indicates the measured flux for a filter masked during SED fitting. In this case, the B -band was masked out since it includes the Ly α emission line. Our imaging data constrain the 4000 Å break and rest-optical colors. (Top-right): 5'' square image cutout for the source in the F160W *HST* filter. The pink cross indicates the source position, and the blue plus sign and dashed blue circle indicate the detection position and the FWHM of the HETDEX fiber PSF. (Bottom-right): 1D extracted spectrum for this source, centered on an 80 Å window around the Ly α emission line. The solid green line indicates the HETDEX Gaussian model fit to the data.

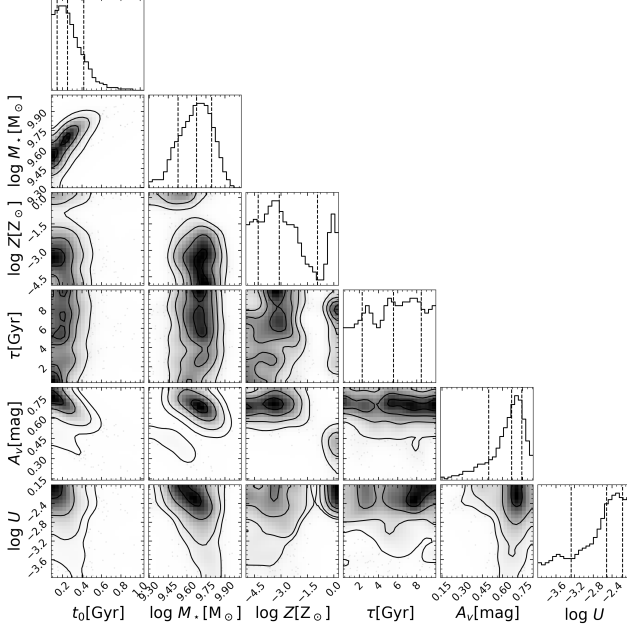


Figure 10. A “corner” plot of the fit in Figure 9 for object ID 10388. The 1D histograms are shown on the diagonal for the posterior distribution of each free parameter in our model (see Table 1). The 2D histograms show the correlations of all parameters with one another, where contour lines are drawn for each σ level. With our broadband photometry, we constrained ages, masses, and dust extinctions well.

4.1. SED-Derived Properties

Figure 11 shows the 1D distributions of posterior median values of stellar mass (M_\star), star formation rate

(SFR), specific star formation rate (sSFR), dust extinction (A_V), mass-weighted age, and UV-slope (β) for all objects in our final LAE sample. We found the median stellar mass of our HETDEX LAEs to be $0.8^{+2.9}_{-0.5} \times 10^9 M_\odot$. This stellar mass value lies near the median masses of LAEs selected in narrowband imaging surveys covering redshifts similar to this study (e.g. Guaita et al. 2011, Gawiser et al. 2007, Vargas et al. 2014, Kusakabe et al. 2018, Santos et al. 2020) and well below typical masses of Lyman-break selected objects (e.g. Shapley et al. 2003, Papovich et al. 2001, Trainor et al. 2019), which often have minimum masses an order of magnitude larger due to the depth of the broadband imaging used in their selection.

We used our SED fitting procedure to obtain the attenuation in the V -band of starlight due to dust for galaxies in the sample, and we obtained a median value of $A_V \sim 0.3$ mag. The presence of dust has been measured in many other samples of LAEs with values of A_V or $E(B-V)$ often falling within a factor of two of this study (e.g. Guaita et al. 2011, Finkelstein et al. 2009, Hathi et al. 2016, Kusakabe et al. 2018, Matthee et al. 2021).

Similar to dust reddening, our LAE sample has similar ages and star formation rates to LAE samples in the literature compiled using narrow band or continuum selection methods. Our SED-derived mass-weighted ages, typically spanning 0.05–0.5 Gyr, broadly agree with the narrow band samples of Acquaviva et al. (2011), Finkelstein et al. (2009), Gawiser et al. (2007), and Vargas

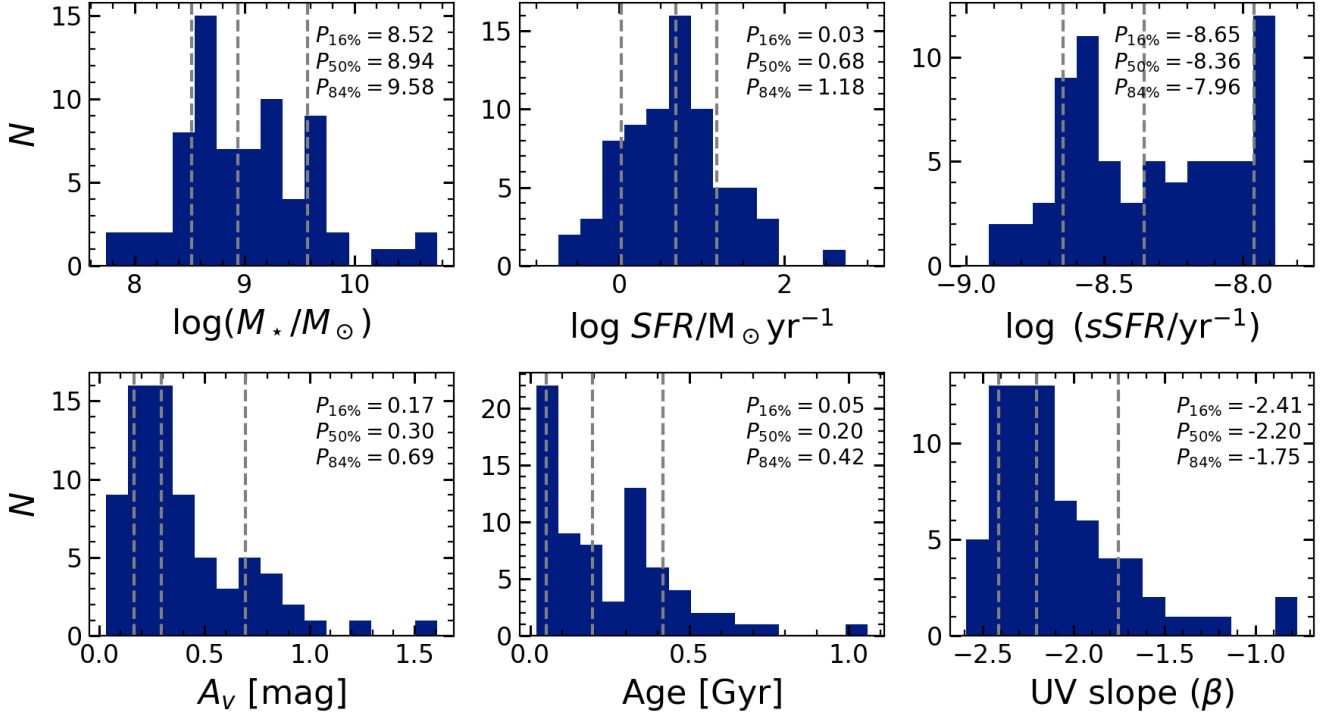


Figure 11. The distributions of posterior median values for (clockwise from top left) stellar mass, SFR, sSFR, dust extinction (in V-band mag), mass-weighted age, and UV-slope for all objects in the sample. The 16th, 50th, and 84th percentiles are indicated by vertical dashed grey lines, and their values are indicated with text in the same units as the x-axis labels. The LAEs in our sample exhibit average properties similar to other LAE samples compiled at comparable redshifts using narrow band selection.

et al. (2014). Our median SFR, $4.8 M_\odot/\text{yr}$, falls near values reported by Gawiser et al. (2007), Hathi et al. (2016), and Kusakabe et al. (2018), but falls 1 dex above the median SFR for LAEs found in the MUSE HUDF Survey (Feltre et al. 2020). This discrepancy does not surprise us since the MUSE HUDF LAE sample had a median mass roughly 0.5 dex lower than this study, and their sample spanned $2.9 < z < 4.6$, probing an era of lower star formation activity in the Universe than the one studied here (see Madau & Dickinson 2014).

Our model included stellar metallicity and ionization parameter as free parameters, but our broadband photometric data could not constrain those values precisely (see Figure 10), since reliable estimates typically require sensitive emission line diagnostics (e.g. Reddy et al. 2021), which were coarsely probed at best by our filter set. For this reason, we do not present or discuss our galaxies' metallicities or ISM ionization conditions, but we note that by letting these parameters vary, our posterior constraints on all other parameters include the uncertainties in these quantities.

4.2. $W_\lambda(\text{Ly}\alpha)$ Distribution

The equivalent width distribution of LAEs has been modeled by various authors as exponential with the form given by Equation 5 (e.g. Gronwall et al. 2007, Guaita et al. 2010, Wold et al. 2014, Jung et al. 2018).

$$\frac{dN}{dW_\lambda} \propto e^{-W_\lambda/W_0} \quad (5)$$

We show our sample's rest-frame $W_\lambda(\text{Ly}\alpha)$ distribution in Figure 12 with an *e*-folding scale $W_0 = 100 \text{ \AA}$ drawn for comparison. We cannot measure the underlying distribution for LAEs from our sample since we have not measured the completeness as a function of equivalent width (which is complex due to our method of sample creation, and not crucial for our study of stellar population properties). Various other studies have precisely measured the Lyman-alpha equivalent width distribution, such as Gronwall et al. (2007), who found an *e*-folding scale of $76^{+11}_{-8} \text{ \AA}$ for a deep, narrow-band (NB) selected LAE sample at $z = 3.1$, Guaita et al. (2010), who measured $W_0 = 50 \pm 7 \text{ \AA}$ for a NB sample at $z = 2.1$, and recently Santos et al. (2020), who measured $W_0 = 129 \pm 11 \text{ \AA}$ for the full SC4K sample at $2 < z < 6$. We plot some of these measured distributions in Figure 12 to show that all are roughly consistent with

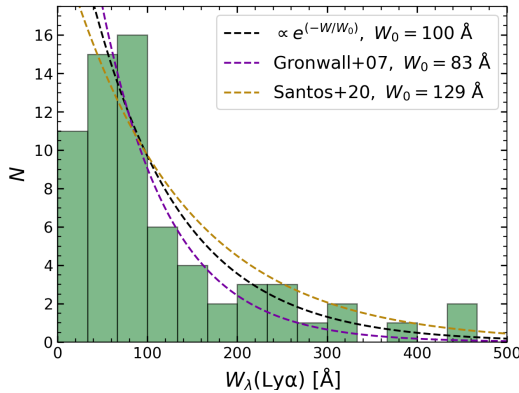


Figure 12. The equivalent width distribution of LAEs in the sample. An exponential distribution with $W_0 = 100 \text{ \AA}$ is drawn in red for comparison, as well as models fit by Gronwall et al. (2007) and Santos et al. (2020). Our data favor models with larger values of W_0 to best match the number of high-EW sources.

our data, though the number of sources in our sample with $W_\lambda(\text{Ly}\alpha) > 200 \text{ \AA}$ favors models with larger e -folding scales. Nonetheless, since small uncertainties in the continuum brightness can scatter equivalent widths to large values, it is worth noting that the lower equivalent width range of the distribution favors models with smaller e -folding scales. It is also apparent that our sample becomes increasingly incomplete at $\text{EW} \lesssim 50 \text{ \AA}$, due to a combination of the HETDEX flux limit, the emission-line identification process, and our counterpart selection process.

4.3. Correlations between $W_\lambda(\text{Ly}\alpha)$ and Galaxy Properties

We combined our SED-derived galaxy properties with the $W_\lambda(\text{Ly}\alpha)$ measurements described above in order to assess correlations between Ly α emission and global galaxy properties. We used $W_\lambda(\text{Ly}\alpha)$ as a proxy for the fraction of photons emitted as Ly α as opposed to $L_{\text{Ly}\alpha}$, for example, because the equivalent width more closely probes the physics governing Ly α escape, whereas the flux also includes physics related to the Ly α production rate. Figure 13 shows M_* , specific star formation rate (sSFR), star formation rate (SFR), dust extinction (A_V), mass-weighted stellar population age, and UV-slope (β) plotted against each galaxy's $W_\lambda(\text{Ly}\alpha)$ measurement. In the figure, error bars denote the 16th to 84th percentile range, and we indicate Pearson's linear correlation coefficient, r_p , and its significance (p -value) with text.

Stellar mass and star formation rate both correlate strongly with $W_\lambda(\text{Ly}\alpha)$, with low mass, low SFR sys-

tems achieving larger $W_\lambda(\text{Ly}\alpha)$ than higher mass systems. The correlation with mass has been established in the literature from studies of a wide variety of galaxies such as LBGs, oELGs, and LAEs. It was noticed early by Ando et al. 2006 and measured recently by many works such as Du et al. 2018, Marchi et al. 2019, Oyarzún et al. 2017, and Shimakawa et al. 2017. Specifically, Weiss et al. (2021) found a negative correlation between the Ly α escape fraction, $f_{\text{esc}}^{\text{Ly}\alpha}$, and stellar mass using data from the HETDEX survey. Additionally, Khostovan et al. (2021) found an intrinsic, negative correlation between H α equivalent width and galaxy stellar mass from a NB survey at $z \sim 5$. While the lack of low-EW, low-mass systems can be driven by selection incompleteness, we should be complete to high-mass, high-EW systems, yet these are seemingly rare.

Notably, our results show no significant anti-correlation between $W_\lambda(\text{Ly}\alpha)$ and dust extinction (A_V), whereas numerous other studies of Lyman-alpha emission measured a clear relationship that indicates dust hinders the ability of the Ly α photon to escape the galaxy. For example, Shapley et al. (2003), Guaita et al. (2011), Du et al. (2018), Hathi et al. (2016), Huang et al. (2021), Marchi et al. (2019), Matthee et al. (2016), Reddy et al. (2021), Trainor et al. (2019), and Weiss et al. (2021), all showed that dustier galaxies exhibit weaker Lyman-alpha emission measured as $W_\lambda(\text{Ly}\alpha)$ or have smaller $f_{\text{esc}}^{\text{Ly}\alpha}$. However, the lack of a significant anti-correlation may be due to our limited sample size and small dynamic range in dust attenuation. Moreover, objects with significant amounts of dust that suppress their Ly α fluxes would not become members of our science sample in the first place. The majority of our sample has $A_V < 0.3$. We do observe multiple galaxies with $A_V > 0.5$, and interestingly these do not all have low $W_\lambda(\text{Ly}\alpha)$, implying that Ly α can escape even from modestly dusty galaxies, which could indicate enhanced escape due to outflows (e.g., Steidel et al. 2010, Erb et al. 2012) or a multi-phase ISM (e.g. Finkelstein et al. 2009, Neufeld 1991).

Our Pearson correlation coefficient suggests a moderate correlation between $W_\lambda(\text{Ly}\alpha)$ and galaxy stellar mass-weighted age ($r_p = 0.32$) in the sense that older galaxies exhibit larger $W_\lambda(\text{Ly}\alpha)$. Marchi et al. (2019) found a similar result, obtaining a Spearman rank correlation coefficient of 0.40. This contrasts with Pentericci et al. (2009) and Pentericci et al. (2010) who found no strong dependence of Ly α equivalent width on age for LAEs and LBGs, as well as Reddy et al. (2021) who found a weak negative correlation between the two measurements for star-forming galaxies in the same redshift range probed by this study.

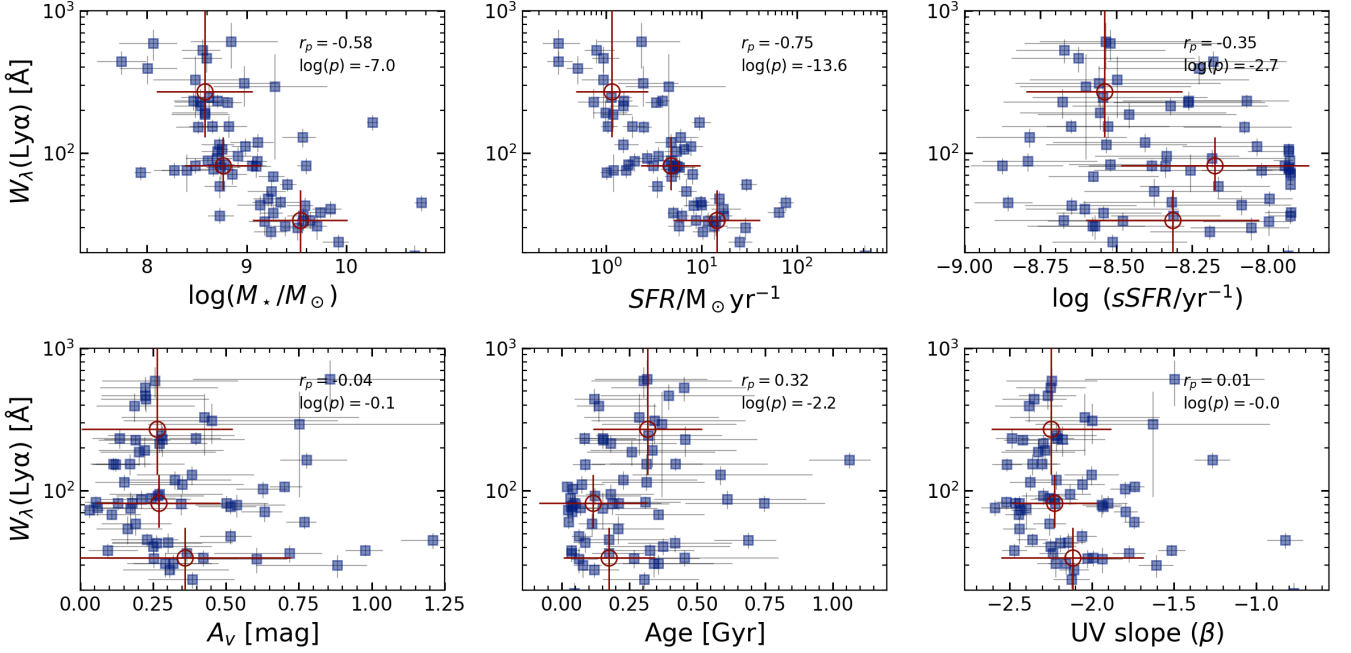


Figure 13. The relationship between $W_\lambda(\text{Ly}\alpha)$ and (clockwise from top left) stellar mass, SFR, sSFR, dust extinction (A_V), mass-weighted age, and UV-slope (β) for all objects in the sample. Grey lines indicate the $\pm 1\sigma$ error bars on physical properties and equivalent width. Open red circles show medians and standard deviations for properties in equivalent width bins having equal numbers of objects. Pearson correlation coefficients, r_p , and p -values are indicated for each plot. Stellar mass and SFR exhibit the strongest correlations with $W_\lambda(\text{Ly}\alpha)$, while age and sSFR correlate moderately. Surprisingly, no strong correlation exists with dust extinction.

Finally, a moderate negative correlation exists between sSFR and $W_\lambda(\text{Ly}\alpha)$, though the large error bars for our measurements of sSFR weaken the reliability of the correlation. For comparison, Hathi et al. (2016) found no significant correlation between the two properties for a sample including Ly α in absorption and emission.

We also plot SFR against M_* for all objects in our sample in Figure 14 to see how our galaxies compare to other objects at similar redshift in relation to the star-forming main sequence (SFMS). We include the best-fit line found by Sanders et al. (2018) for star-forming galaxies in the MOSDEF survey at $z \sim 2.3$. Note that masses derived for that study used the Chabrier (2003) IMF and Calzetti et al. (2000) dust curve but stellar population synthesis models from Conroy et al. (2009). We also use a colorbar to show the value of $W_\lambda(\text{Ly}\alpha)$ for each galaxy. The position of LAEs on the SFMS remains somewhat controversial. Studies such as Vargas et al. (2014), Finkelstein et al. (2015), Hagen et al. (2016), and Santos et al. (2020) found LAEs to lie above the relation, while other studies have interpreted them as lying directly on the low-mass end of the relation (e.g. Kusakabe et al. 2018). Figure 14 shows that the LAEs in our sample lie largely on the SFMS, though a significant

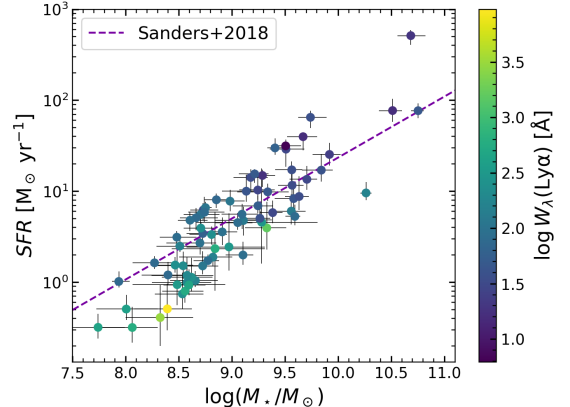


Figure 14. The stellar mass - star formation rate correlation for LAEs in our sample. The trend fit by Sanders et al. (2018) for $z \sim 2.3$ star-forming galaxies is drawn in dashed purple for comparison. LAEs in our sample largely fall on the SFMS, though the lowest mass sources ($M_* < 10^9 M_\odot$) tend to fall below the relation.

fraction lie below the relation of Sanders et al. (2018) for $M_* < 10^9 M_\odot$.

In Appendix A, we explore the model-dependence of our measured galaxy properties, since the parameters derived from SED fitting can be systematically different using different models (see Conroy 2013). We conclude

926 that our results, including the median physical properties
 927 and the correlations with $W_{\lambda}(\text{Ly}\alpha)$ are not driven
 928 by our specific choice of model.

929 5. DISCUSSION

930 5.1. Are HETDEX LAEs Special?

931 The question, “What is a HETDEX LAE?” holds par-
 932 ticular importance for astronomers studying galaxy sci-
 933 ence with this survey. A vast sample of HETDEX LAEs
 934 is upcoming, and samples of such objects selected by
 935 emission line detection from a blind spectroscopic survey
 936 remain rare in the literature (with the exception of the
 937 HETDEX Pilot Survey (Adams et al. 2011, Blanc et al.
 938 2011), which probed a smaller area to a brighter flux
 939 limit, and MUSE surveys, which probe much smaller
 940 areas to fainter flux limits with only a small overlap
 941 in redshift with HETDEX). Characterizing any idiosyn-
 942 crasies in the HETDEX LAE population will put these
 943 objects in context relative to the numerous LAEs found
 944 by previous studies, and it will aid the interpretation of
 945 future blind spectroscopic surveys for these objects in
 946 the EoR.

947 As described above, in our $f_{\text{Ly}\alpha} \gtrsim 6 \times$
 948 $10^{-17} \text{ erg s}^{-1} \text{ cm}^{-2}$ flux-limited sample (Gebhardt et al.
 949 2021), the median galaxy mass of $0.8^{+2.9}_{-0.5} \times 10^9 \text{ M}_\odot$
 950 lies very close to many LAE samples selected through
 951 narrow band imaging. For example, Gawiser et al.
 952 (2007) found a median mass of $1^{+0.6}_{-0.4} \times 10^9 \text{ M}_\odot$ with
 953 a flux limit of $1.5 \times 10^{-17} \text{ erg s}^{-1} \text{ cm}^{-2}$ at $z = 3.1$.
 954 Guaita et al. (2011) pushed to an even lower median
 955 mass of $\sim 4 \times 10^8 \text{ M}_\odot$, roughly a factor of two less
 956 massive than this sample’s median, with a flux limit of
 957 $2.0 \times 10^{-17} \text{ erg s}^{-1} \text{ cm}^{-2}$ at $z = 2.1$. The MUSE HUDF
 958 went even deeper, finding sources at $z > 3$ with Ly α line
 959 fluxes as small as $\sim 2 \times 10^{-18} \text{ erg s}^{-1} \text{ cm}^{-2}$ and obtain-
 960 ing a median sample mass of $\sim 2.5 \times 10^8 \text{ M}_\odot$. The sam-
 961 ple of Santos et al. (2020) was limited by medium-band
 962 line flux limits spanning $3.0 - 4.8 \times 10^{-17} \text{ erg s}^{-1} \text{ cm}^{-2}$
 963 over $2 < z < 6$ (Sobral et al. 2018) and measured a me-
 964 dian LAE mass of $2 \times 10^9 \text{ M}_\odot$, consistent with this study.
 965 Of course, the mass range probed by HETDEX falls far
 966 below samples selected using the Lyman/Lyman-alpha
 967 break (for example, the lowest mass probed by Papovich
 968 et al. (2001) was 10^{10} M_\odot at $2.0 < z < 3.5$). Thus, the
 969 HETDEX flux limit explores an LAE mass range com-
 970 parable to NB surveys, yet slightly more massive than
 971 the deepest NB and spectroscopic surveys. At the ex-
 972 pense of sensitivity, the HETDEX survey can find fairly
 973 low-mass LAEs over a large continuous redshift interval,
 974 reducing the effects of cosmic variance compared to NB
 975 observations.

976 As mentioned in §4.1, the LAEs in this sample do not
 977 stand out from NB samples at similar redshift in terms
 978 of age, star formation rate, and dust extinction. Thus,
 979 we can conclude that the HETDEX survey selects a typ-
 980 ical LAE having properties consistent with the general
 981 NB-selected population, but it may have slightly higher
 982 stellar mass based on the line flux limit of the survey.

983 Nonetheless, our sample may stand out in its relation
 984 to the SFR- M_\star relation shown in Figure 14. Compared
 985 to the relation measured in Sanders et al. (2018), LAEs
 986 in the sample with $M_\star \lesssim 10^9 \text{ M}_\odot$ appear to lie below the
 987 trend. This contrasts markedly with the work of Hagen
 988 et al. (2016), who compiled their sample using the HET-
 989 DEX Pilot survey (Adams et al. 2011, Blanc et al. 2011)
 990 and found their LAEs to lie above the SFMS. Interest-
 991 ingly, the LAEs lying below the SFMS in Figure 14 have
 992 very high $W_{\lambda}(\text{Ly}\alpha)$, which correlates with lower M_\star and
 993 SFR in Figure 13. We are not surprised that the low-
 994 est mass systems in our sample have the highest values
 995 of $W_{\lambda}(\text{Ly}\alpha)$ given the negative correlation with M_\star and
 996 the fact that low mass objects need large $W_{\lambda}(\text{Ly}\alpha)$ to
 997 be detected by HETDEX, but their position below the
 998 SFMS is peculiar. It could be related to the weak nega-
 999 tive correlation we found between $W_{\lambda}(\text{Ly}\alpha)$ and sSFR,
 1000 or could simply be an artifact of our small sample size.
 1001 This motivates further study of the positions of LAEs
 1002 on the SFMS with larger samples.

1003 5.2. Which Properties Drive Ly α Emission?

1004 While the size of the sample analyzed in this study is
 1005 small, we were still able to extract important informa-
 1006 tion linking galaxy stellar-population properties to Ly α
 1007 emission strength. As the number of LAEs detected by
 1008 HETDEX grows in fields with rich photometric data,
 1009 such as the Spitzer-HETDEX Exploratory Large-Area
 1010 Survey (SHELA) (Papovich et al. 2016), the number
 1011 of LAEs with measured galaxy properties will grow by
 1012 many orders of magnitude. This will provide a trove
 1013 of useful data for explaining why some galaxies shine
 1014 brightly in Ly α while others do not, as well as exploring
 1015 the effects of galaxy environment on Ly α emission.

1016 We found a significant, strong negative correlation be-
 1017 tween $W_{\lambda}(\text{Ly}\alpha)$ and stellar mass in our sample (see the
 1018 top left panel of Figure 13). This trend is often theoret-
 1019 ically attributed to low mass, star-forming galaxies hav-
 1020 ing less neutral gas to resonantly scatter the Ly α pho-
 1021 ton (as well as less dust) leading to a shorter total path
 1022 length to exit the galaxy without absorption by dust (see
 1023 Ando et al. 2006). In this sample, $W_{\lambda}(\text{Ly}\alpha)$ also nega-
 1024 tively correlated (even more strongly) with SFR, and the
 1025 fact that stellar mass and star formation rate correlate
 1026 strongly with each other complicates the interpretation

of this result. Weiss et al. (2021) addressed this issue by binning their sample of [O III]-emitting galaxies with Ly α line flux measurements from HETDEX according to stellar mass and SFR. They found mass to better predict $f_{esc}^{Ly\alpha}$ at fixed SFR than SFR did at fixed mass.

Fascinatingly, we did not find even a weak correlation between dust extinction and $W_\lambda(Ly\alpha)$. This seems surprising given that many authors have noted such a correlation and that the theoretical explanation is inarguable: resonantly scattered Ly α photons can get absorbed readily in the presence of even a small amount of dust. A partial explanation for our sample’s behavior with A_V could be that it consists of systems exhibiting strong Ly α emission, not absorption. For example, Reddy et al. (2021) studied systems with Ly α in net absorption or emission and found a strong correlation between $W_\lambda(Ly\alpha)$ and $E(B - V)$. If our sample contained objects with negative $W_\lambda(Ly\alpha)$, perhaps those objects would reveal the correlation. Nevertheless, other studies of only emitters ($W_\lambda(Ly\alpha) > 0$) have also noted a trend with dust extinction, such as Marchi et al. (2019). This interpretation may be complicated by the Ly α photon’s ability to escape the galaxy even in the presence of large amounts of dust. Given a clumpy ISM geometry, clumps of gas and dust can act as mirrors to Ly α photons, which “bounce” off the surfaces of these clumps through resonant scattering by neutral gas, while continuum photons pass through and thus experience extinction. Gronke et al. (2016) found that simulated Ly α emission lines agreed well with observations for models with clumpy ISM geometries, and Finkelstein et al. (2009) found that clumpy-ISM models better fit the SEDs of over half their NB-selected sample of LAEs at $z \sim 4.5$. Vargas et al. (2014) also found their sample of 20 NB-selected LAEs at $z=2.1$ favored clumpy-ISM models.

Lastly, we found a moderate correlation between $W_\lambda(Ly\alpha)$ and galaxy mass-weighted age. The strength of Ly α emission depends on both its production through recombination in HII regions as well as its escape through channels in the ISM with low neutral gas covering fractions, so the interplay between these processes determines $W_\lambda(Ly\alpha)$. As noted by Marchi et al. (2019), who obtained a similar result, the trend with age could arise from older systems having experienced intense star formation in their past, where stellar winds and radiation cleared out neutral gas and dust, leaving channels for Ly α escape. Through ongoing star formation or recent bursts, these objects can still produce Ly α photons, and the ISM conditions favor their escape. For the youngest galaxies, even though the most massive, ionizing photon-producing stars are present, it is possible

that a significant amount of dust and neutral gas has yet to be swept away, hindering the escape of Ly α .

6. PREDICTING LYMAN-ALPHA EMISSION IN THE EPOCH OF REIONIZATION

Using our knowledge of Ly α emission from HETDEX galaxies situated in an ionized IGM, we can attempt to predict the intrinsic emission strength of LAEs at $z > 7$, an era where starlight from galaxies was still actively reionizing the universe.

6.1. An LAE Sample in the Epoch of Reionization

Our sample at $1.9 < z < 3.5$ provides a view of Ly α emission unobscured by a significant IGM neutral fraction. By creating a predictive model that connects global galaxy properties to their intrinsic $W_\lambda(Ly\alpha)$ in this pristine era, we can apply it to LAEs in the EoR to derive their expected intrinsic $W_\lambda(Ly\alpha)$, then attributing any deficiency of Ly α emission from objects in the EoR to an increasing neutral fraction. This does require the assumption that the production and escape of Ly α photons does not evolve with redshift for fixed galaxy properties, which will require further testing. As a pilot attempt here, we took advantage of the sample of $z > 7$ LAEs that Jung et al. (2020) found in GOODS-N to test our ability to predict Ly α emission from EoR galaxies.

Using a deep, spectroscopic survey conducted with Keck/MOSFIRE, Jung et al. (2020) found $10 > 4\sigma$ Ly α detections at $z > 7$ among 72 high- z candidate galaxies. Such objects likely reside in ionized bubbles of the IGM, allowing the Ly α photon to redshift away from the resonant-frequency therefore lowering the absorption cross-section with neutral hydrogen. These emitters thus serve as direct tests of our understanding of the galaxy properties that modulate Ly α emission strength from the ISM/CGM.

Because the photometric catalog for the GOODS-N field contains the LAEs discovered by Jung et al. (2020), we performed the same SED analysis detailed in section 3.1 for those objects. We again masked all photometric bands including and blueward of Ly α given the object’s spectroscopic redshift. For most of the $z > 7$ LAEs, this left 3 *HST* filters as well as both *Spitzer*/IRAC channels. We again used BAGPIPES to estimate the galaxy properties, adopting our fiducial model (delayed- τ SFH, Calzetti et al. 1994 dust law). Figure 15 shows an example fit for an object at $z = 7.51$.

6.2. A Predictive Model for $W_\lambda(Ly\alpha)$

To predict the Ly α equivalent widths of the $z > 7$ sample, we chose several properties that strongly impact the emergent Ly α emission from galaxies: stellar

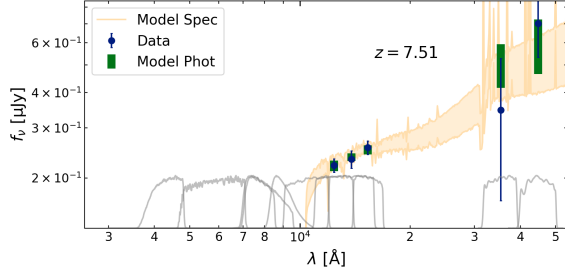


Figure 15. An example BAGPIPES SED fit for LAE ID z7_GND_42912 at $z = 7.51$ detected by Jung et al. (2020). For scaling purposes, we do not show the upper-limits for non-detections in the *HST* bands blueward of the Ly α break. From our photometric data, we constrained the stellar population properties of ten LAEs in the EoR, allowing us to predict their intrinsic Ly α emission using our HETDEX sample.

mass, dust extinction, and star formation rate. As discussed above, stellar mass may determine the amount of neutral hydrogen gas (and thus dust) in the galaxy as well as the total path length needed to escape. In the presence of dust, Ly α photons may terminate their resonant scattering process through absorption by a dust grain following re-emission at longer wavelengths, limiting likelihood of escape. Finally, the global star formation rate impacts the production of UV photons that can create Ly α through recombination, and feedback from star formation may impact the structure of the ISM itself, creating ionized channels for escape.

Using the posterior distributions sampled by BAGPIPES, we matched each $z > 7$ emitter to LAEs in the HETDEX sample based on SED-derived properties. To do this, we calculated the “separation” in the log mass, SFR, dust attenuation parameter space from the EoR LAEs to each LAE in the HETDEX sample. For the separation calculation, we divided each parameter value by the full range of values in the sample to normalize the parameter space. For example, for log stellar mass, an object in the HETDEX sample with log mass halfway between the sample minimum and maximum would have a value of 0.5, so the difference between 0.5 and the EoR LAE log stellar mass scaled the same way would become input to the Euclidean distance formula. We then ranked the HETDEX LAEs by separation in parameter space and constructed the prediction using the $N = 3, 5$, and 7 closest neighbors. We computed the posterior $W_\lambda(\text{Ly}\alpha)$ distribution by co-adding Gaussian distributions with mean and standard deviation set by the $W_\lambda(\text{Ly}\alpha)$ measurements and error bars in our sample. To give more importance to those LAEs that closely resembled the EoR galaxy, we weighted each Gaussian distribution by the inverse of its squared distance in parameter space from the EoR galaxy when co-adding to

obtain the final prediction. The predicted $W_\lambda(\text{Ly}\alpha)$ distributions are normalized such that the integral over all equivalent widths equals unity.

Figure 16 shows our predicted $W_\lambda(\text{Ly}\alpha)$ distributions for LAEs in the Jung et al. (2020) sample with Ly α $S/N > 4$. We show predictions using three different values of N , the number of nearest neighbors in parameter space, to reveal any stochasticity in the prediction. The measured Ly α equivalent widths from Jung et al. (2020) are indicated by vertical dashed lines with 1σ error intervals shaded grey. Importantly, we only expect our predictions to match the observed equivalent widths of EoR LAEs if they exist in ionized bubbles. If the EoR LAEs instead exist in regions of the IGM with significant neutral fractions, we expect to over-predict the Ly α emission. On the other hand, an under-prediction of the Ly α emission from an EoR object would imply our sample size is too small to account for the diversity in physical properties of the LAE population.

Referring to Figure 16, in five out of ten cases (ID z7_GND_18626, z7_GND_44088, z7_GND_42912, z7_GND_16863, and z7_GND_39781) our predictions matched well. For strong emitters ($W_\lambda(\text{Ly}\alpha) > 20 \text{ \AA}$), our prediction fell within 2σ of the measured value five out of eight times. Furthermore, two strong emitters (z7_GND_42912 and z7_GND_16863), postulated by Jung et al. (2020) to inhabit ionized bubbles, had observed equivalent widths greater than or equal to the majority of our predicted $W_\lambda(\text{Ly}\alpha)$ distributions, as one might expect for sources with little IGM attenuation. We are not surprised that our model failed to predict weak Ly α emission accurately since our sample by construction contains far more strong emitters than weak ones (see Figure 12), and over-prediction of Ly α emission strength in EoR galaxies could very well result from absorption of Ly α photons by neutral hydrogen in the IGM instead of ISM/CGM effects. We grossly underpredicted the emission from ID z7_GND_34204, which could be attributed to the dearth of objects in our sample with very high equivalent widths to match with that object’s value, $\sim 280 \text{ \AA}$. ID z7_GND_42912 offers a good example of how challenging predicting Ly α emission can be. As N increases, the peak of the predicted distribution shifts from agreeing well with the observation to under-predicting it. It is clear that our sample is presently too small to fully span the parameter space in both $W_\lambda(\text{Ly}\alpha)$ and physical properties. Future analyses with much larger samples made possible by HETDEX should be able to better capture the mean trends as well as variance in galaxy parameters that determine Ly α emission strength.

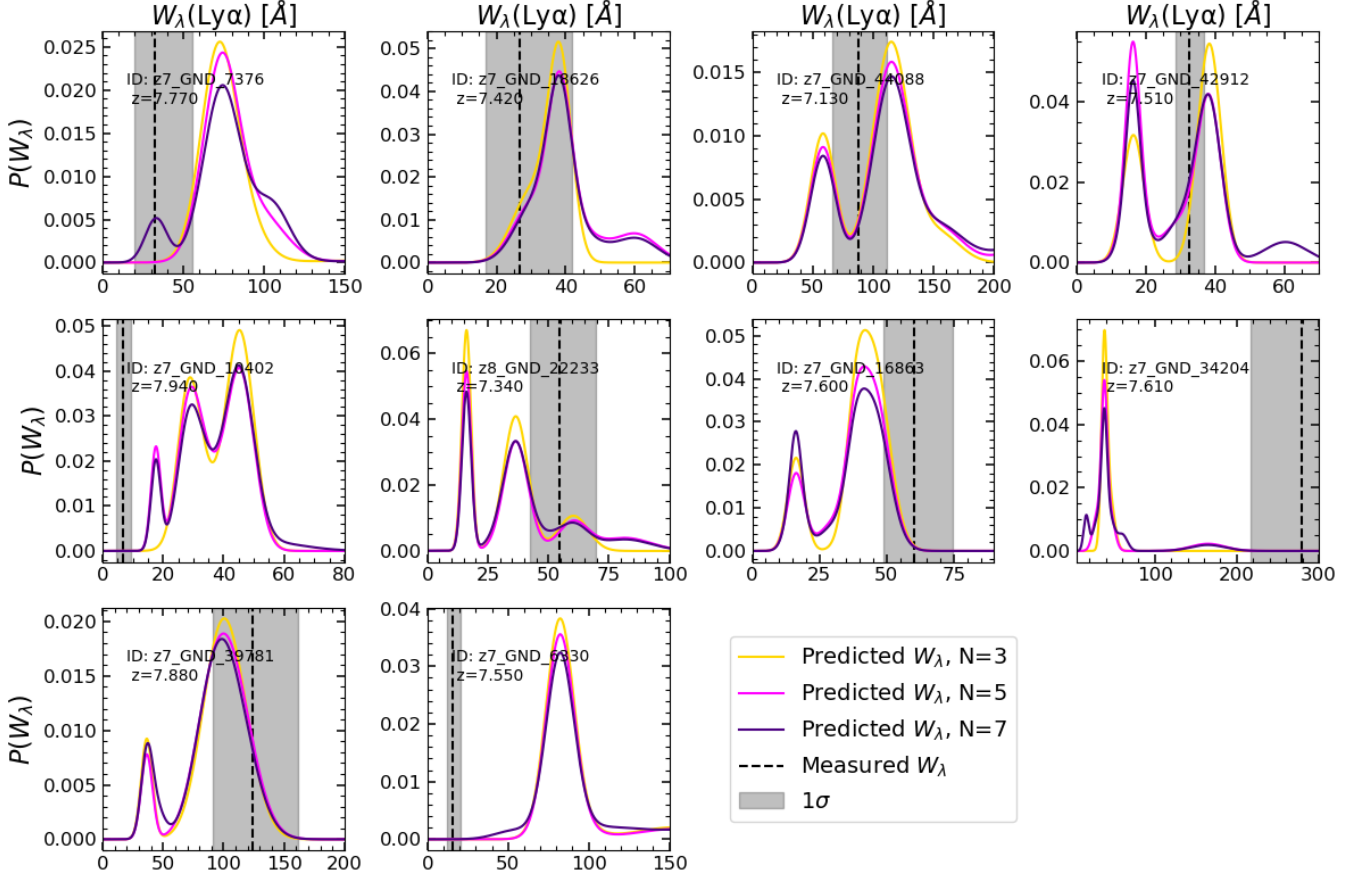


Figure 16. Probabilistic predictions of $W_\lambda(\text{Ly}\alpha)$ for ten LAEs at $z > 7$ having emission line $S/N > 4$. The distributions were normalized by setting their integrals to unity. We chose stellar mass, SFR, and dust extinction as predictive properties for this calculation. Gold, magenta, and indigo lines show the probability distribution of our predictions using $N=3, 5$, and 7 nearest neighbors, and the gray shaded region shows the 68% confidence interval for the equivalent width measurements from Jung et al. (2020). Object IDs and redshifts are indicated with text for each plot. We find good agreement between prediction and observation for the majority of strong emitters

Many of the predictions in Figure 16 bode well for constraining the expected $W_\lambda(\text{Ly}\alpha)$ given a suite of galaxy properties measured from broadband SED fitting. With larger samples that suffer less from the inherent idiosyncratic behavior of Ly α emission (for example, its dependence on the observer's line-of-sight), a rigorous, statistical understanding of the properties that drive that emission will arise, unlocking the potential of LAEs to probe cosmic reionization. We further note that, with larger samples, machine learning (ML) may prove an invaluable tool in making the nuanced connection between global galaxy properties and Ly α emission strength, as the problem requires a regression analysis well suited for ML techniques.

7. SUMMARY

We used SED fitting to study the properties of a sample of LAEs from the HETDEX survey in GOODS-N to better understand the phenomenology behind Ly α

emission and ultimately leverage these beacons of light in the distant Universe as probes of cosmic reionization.

To build the sample, we inspected 842 emission line detections to determine if the line was Ly α or a feature from a low-redshift galaxy, such as [O II]. We then created a procedure to synthesize information about angular separation from the emission line detection position, extracted emission line flux, and χ^2 of SED fit assuming $z_{\text{Ly}\alpha}$ to identify the continuum counterpart in our deep, mult-band *HST* imaging in GOODS-N. After removing detections with no counterparts, AGN contaminants, and sources with insufficient photometric data, we analyzed a sample of 72 LAEs using SED fitting performed by BAGPIPES.

Our sample's properties were consistent with studies of LAEs from NB imaging surveys at similar redshifts. Our median sample mass was $0.8^{+2.9}_{-0.5} \times 10^9 M_\odot$, and the galaxies' SFRs appeared to put them approximately on the star-forming main sequence, except for

at $M_\star < 10^9 M_\odot$. Using Ly α emission line flux measurements from HETDEX, we also studied correlations between $W_\lambda(\text{Ly}\alpha)$ and galaxy properties. We found strong correlations between $W_\lambda(\text{Ly}\alpha)$ and stellar mass as well as SFR. We additionally found a moderate correlation where galaxies with older stellar populations had larger Ly α equivalent widths. Interestingly, we did not find a significant impact of dust extinction on $W_\lambda(\text{Ly}\alpha)$, whereas many other studies have. Overall, this paints a picture of LAEs as low-mass systems with moderate star formation activity wherein Ly α photons can escape even in the presence of dust. Also, the LAEs detected by HETDEX do not stand out significantly in terms of their stellar population properties from LAEs found using NB imaging with comparable flux limits.

Finally, we used our LAE sample to try to predict the value of $W_\lambda(\text{Ly}\alpha)$ for ten LAEs at $z > 7$ by matching the distinct samples in the parameter space of mass, SFR, and dust extinction. Our prediction matched the data well 5/10 times, but three over-predictions could simply be the result of neutral hydrogen in the IGM attenuating the flux. With large sample sizes and tools such as machine learning, we are optimistic about the ability of HETDEX LAEs to unlock the potential of Ly α as a reliable reionization probe.

8. ACKNOWLEDGEMENTS

APM and SLF acknowledge support from the National Science Foundation, through grants AST-1908817 and AST-1614798.

HETDEX is led by the University of Texas at Austin McDonald Observatory and Department of Astronomy with participation from the Ludwig-Maximilians-Universität München, Max-Planck-Institut für Ex-

traterrestrische Physik (MPE), Leibniz-Institut für Astrophysik Potsdam (AIP), Texas A&M University, Pennsylvania State University, Institut für Astrophysik Göttingen, The University of Oxford, Max-Planck-Institut für Astrophysik (MPA), The University of Tokyo and Missouri University of Science and Technology. In addition to Institutional support, HETDEX is funded by the National Science Foundation (grant AST-0926815), the State of Texas, the US Air Force (AFRL FA9451-04-2-0355), and generous support from private individuals and foundations.

The observations were obtained with the Hobby-Eberly Telescope (HET), which is a joint project of the University of Texas at Austin, the Pennsylvania State University, Ludwig-Maximilians-Universität München, and Georg-August-Universität Göttingen. The HET is named in honor of its principal benefactors, William P. Hobby and Robert E. Eberly.

VIRUS is a joint project of the University of Texas at Austin, Leibniz-Institut für Astrophysik Potsdam (AIP), Texas A&M University (TAMU), Max-Planck-Institut für Extraterrestrische Physik (MPE), Ludwig-Maximilians-Universität München, Pennsylvania State University, Institut für Astrophysik Göttingen, University of Oxford, and the Max-Planck-Institut für Astrophysik (MPA).

The authors acknowledge the Texas Advanced Computing Center (TACC) at The University of Texas at Austin for providing high performance computing, visualization, and storage resources that have contributed to the research results reported within this paper. URL: <http://www.tacc.utexas.edu>

The Institute for Gravitation and the Cosmos is supported by the Eberly College of Science and the Office of the Senior Vice President for Research at Pennsylvania State University.

REFERENCES

- 1320 Abazajian, K. N., Adelman-McCarthy, J. K., Agüeros, Bertin, E., & Arnouts, S. 1996, A&AS, 117, 393,
- 1321 M. A., et al. 2009, ApJS, 182, 543, doi: [10.1088/0067-0049/182/2/543](https://doi.org/10.1088/0067-0049/182/2/543)
- 1322 Acquaviva, V., Gawiser, E., & Guaita, L. 2011, ApJ, 737, 47, doi: [10.1088/0004-637X/737/2/47](https://doi.org/10.1088/0004-637X/737/2/47)
- 1323 Adams, J. J., Blanc, G. A., Hill, G. J., et al. 2011, ApJS, 192, 5, doi: [10.1088/0067-0049/192/1/5](https://doi.org/10.1088/0067-0049/192/1/5)
- 1324 Ando, M., Ohta, K., Iwata, I., et al. 2006, ApJL, 645, L9, doi: [10.1086/505652](https://doi.org/10.1086/505652)
- 1325 Ashby, M. L. N., Willner, S. P., Fazio, G. G., et al. 2015, ApJS, 218, 33, doi: [10.1088/0067-0049/218/2/33](https://doi.org/10.1088/0067-0049/218/2/33)
- 1326 Atek, H., Kunth, D., Schaefer, D., et al. 2014, A&A, 561, A89, doi: [10.1051/0004-6361/201321519](https://doi.org/10.1051/0004-6361/201321519)
- 1327 1333 Blanc, G. A., Adams, J. J., Gebhardt, K., et al. 2011, ApJ, 736, 31, doi: [10.1088/0004-637X/736/1/31](https://doi.org/10.1088/0004-637X/736/1/31)
- 1328 Bruzual, G., & Charlot, S. 2003, MNRAS, 344, 1000, doi: [10.1046/j.1365-8711.2003.06897.x](https://doi.org/10.1046/j.1365-8711.2003.06897.x)
- 1329 Calzetti, D., Armus, L., Bohlin, R. C., et al. 2000, ApJ, 533, 682, doi: [10.1086/308692](https://doi.org/10.1086/308692)
- 1330 1334 Calzetti, D., Kinney, A. L., & Storchi-Bergmann, T. 1994, ApJ, 429, 582, doi: [10.1086/174346](https://doi.org/10.1086/174346)
- 1331 Cardelli, J. A., Clayton, G. C., & Mathis, J. S. 1989, ApJ, 345, 245, doi: [10.1086/167900](https://doi.org/10.1086/167900)
- 1332

- 1345 Carnall, A. C., McLure, R. J., Dunlop, J. S., & Davé, R.
 1346 2018, MNRAS, 480, 4379, doi: [10.1093/mnras/sty2169](https://doi.org/10.1093/mnras/sty2169)
- 1347 Chabrier, G. 2003, PASP, 115, 763, doi: [10.1086/376392](https://doi.org/10.1086/376392)
- 1348 Charlot, S., & Fall, S. M. 2000, ApJ, 539, 718,
 1349 doi: [10.1086/309250](https://doi.org/10.1086/309250)
- 1350 Conroy, C. 2013, ARA&A, 51, 393,
 1351 doi: [10.1146/annurev-astro-082812-141017](https://doi.org/10.1146/annurev-astro-082812-141017)
- 1352 Conroy, C., Gunn, J. E., & White, M. 2009, ApJ, 699, 486,
 1353 doi: [10.1088/0004-637X/699/1/486](https://doi.org/10.1088/0004-637X/699/1/486)
- 1354 Cowie, L. L., & Hu, E. M. 1998, AJ, 115, 1319,
 1355 doi: [10.1086/300309](https://doi.org/10.1086/300309)
- 1356 Dijkstra, M. 2014, PASA, 31, e040,
 1357 doi: [10.1017/pasa.2014.33](https://doi.org/10.1017/pasa.2014.33)
- 1358 Du, X., Shapley, A. E., Reddy, N. A., et al. 2018, ApJ, 860,
 1359 75, doi: [10.3847/1538-4357/aabfcf](https://doi.org/10.3847/1538-4357/aabfcf)
- 1360 Erb, D. K., Quider, A. M., Henry, A. L., & Martin, C. L.
 1361 2012, ApJ, 759, 26, doi: [10.1088/0004-637X/759/1/26](https://doi.org/10.1088/0004-637X/759/1/26)
- 1362 Farrow, D. J., Sánchez, A. G., Ciardullo, R., et al. 2021,
 1363 MNRAS, 507, 3187, doi: [10.1093/mnras/stab1986](https://doi.org/10.1093/mnras/stab1986)
- 1364 Feltre, A., Maseda, M. V., Bacon, R., et al. 2020, A&A,
 1365 641, A118, doi: [10.1051/0004-6361/202038133](https://doi.org/10.1051/0004-6361/202038133)
- 1366 Feroz, F., & Skilling, J. 2013, in American Institute of
 1367 Physics Conference Series, Vol. 1553, Bayesian Inference
 1368 and Maximum Entropy Methods in Science and
 1369 Engineering: 32nd International Workshop on Bayesian
 1370 Inference and Maximum Entropy Methods in Science and
 1371 Engineering, ed. U. von Toussaint, 106–113,
 1372 doi: [10.1063/1.4819989](https://doi.org/10.1063/1.4819989)
- 1373 Finkelstein, K. D., Finkelstein, S. L., Tilvi, V., et al. 2015,
 1374 ApJ, 813, 78, doi: [10.1088/0004-637X/813/1/78](https://doi.org/10.1088/0004-637X/813/1/78)
- 1375 Finkelstein, S. L., Papovich, C., Giavalisco, M., et al. 2010,
 1376 ApJ, 719, 1250, doi: [10.1088/0004-637X/719/2/1250](https://doi.org/10.1088/0004-637X/719/2/1250)
- 1377 Finkelstein, S. L., Rhoads, J. E., Malhotra, S., & Grogin, N.
 1378 2009, ApJ, 691, 465, doi: [10.1088/0004-637X/691/1/465](https://doi.org/10.1088/0004-637X/691/1/465)
- 1379 Finkelstein, S. L., Papovich, C., Salmon, B., et al. 2012,
 1380 ApJ, 756, 164, doi: [10.1088/0004-637X/756/2/164](https://doi.org/10.1088/0004-637X/756/2/164)
- 1381 Finkelstein, S. L., D’Aloisio, A., Paardekooper, J.-P., et al.
 1382 2019, ApJ, 879, 36, doi: [10.3847/1538-4357/ab1ea8](https://doi.org/10.3847/1538-4357/ab1ea8)
- 1383 Finkelstein, S. L., Bagley, M., Song, M., et al. 2021, arXiv
 1384 e-prints, arXiv:2106.13813.
 1385 <https://arxiv.org/abs/2106.13813>
- 1386 Foreman-Mackey, D. 2016, The Journal of Open Source
 1387 Software, 1, 24, doi: [10.21105/joss.00024](https://doi.org/10.21105/joss.00024)
- 1388 Foreman-Mackey, D., Hogg, D. W., Lang, D., & Goodman,
 1389 J. 2013, PASP, 125, 306, doi: [10.1086/670067](https://doi.org/10.1086/670067)
- 1390 Gaia Collaboration, Brown, A. G. A., Vallenari, A., et al.
 1391 2018, A&A, 616, A1, doi: [10.1051/0004-6361/201833051](https://doi.org/10.1051/0004-6361/201833051)
- 1392 Gawiser, E., Francke, H., Lai, K., et al. 2007, ApJ, 671,
 1393 278, doi: [10.1086/522955](https://doi.org/10.1086/522955)
- 1394 Gebhardt, K., Mentuch Cooper, E., Ciardullo, R., et al.
 1395 2021, arXiv e-prints, arXiv:2110.04298.
- 1396 <https://arxiv.org/abs/2110.04298>
- 1397 Giavalisco, M., Ferguson, H. C., Koekemoer, A. M., et al.
 1398 2004, ApJL, 600, L93, doi: [10.1086/379232](https://doi.org/10.1086/379232)
- 1399 Grogin, N. A., Kocevski, D. D., Faber, S. M., et al. 2011,
 1400 ApJS, 197, 35, doi: [10.1088/0067-0049/197/2/35](https://doi.org/10.1088/0067-0049/197/2/35)
- 1401 Gronke, M., Dijkstra, M., McCourt, M., & Oh, S. P. 2016,
 1402 ApJL, 833, L26, doi: [10.3847/2041-8213/833/2/L26](https://doi.org/10.3847/2041-8213/833/2/L26)
- 1403 Gronwall, C., Ciardullo, R., Hickey, T., et al. 2007, ApJ,
 1404 667, 79, doi: [10.1086/520324](https://doi.org/10.1086/520324)
- 1405 Guaita, L., Gawiser, E., Padilla, N., et al. 2010, ApJ, 714,
 1406 255, doi: [10.1088/0004-637X/714/1/255](https://doi.org/10.1088/0004-637X/714/1/255)
- 1407 Guaita, L., Acquaviva, V., Padilla, N., et al. 2011, ApJ,
 1408 733, 114, doi: [10.1088/0004-637X/733/2/114](https://doi.org/10.1088/0004-637X/733/2/114)
- 1409 Hagen, A., Zeimann, G. R., Behrens, C., et al. 2016, ApJ,
 1410 817, 79, doi: [10.3847/0004-637X/817/1/79](https://doi.org/10.3847/0004-637X/817/1/79)
- 1411 Harris, C. R., Millman, K. J., van der Walt, S. J., et al.
 1412 2020, Nature, 585, 357, doi: [10.1038/s41586-020-2649-2](https://doi.org/10.1038/s41586-020-2649-2)
- 1413 Hathi, N. P., Le Fèvre, O., Ilbert, O., et al. 2016, A&A,
 1414 588, A26, doi: [10.1051/0004-6361/201526012](https://doi.org/10.1051/0004-6361/201526012)
- 1415 Hayes, M. 2015, PASA, 32, e027, doi: [10.1017/pasa.2015.25](https://doi.org/10.1017/pasa.2015.25)
- 1416 Hayes, M., Östlin, G., Duval, F., et al. 2014, ApJ, 782, 6,
 1417 doi: [10.1088/0004-637X/782/1/6](https://doi.org/10.1088/0004-637X/782/1/6)
- 1418 Hill, G. J., Gebhardt, K., Komatsu, E., et al. 2008,
 1419 Astronomical Society of the Pacific Conference Series,
 1420 Vol. 399, The Hobby-Eberly Telescope Dark Energy
 1421 Experiment (HETDEX): Description and Early Pilot
 1422 Survey Results, ed. T. Kodama, T. Yamada, & K. Aoki,
 1423 115
- 1424 Hill, G. J., Lee, H., MacQueen, P. J., et al. 2021, arXiv
 1425 e-prints, arXiv:2110.03843.
 1426 <https://arxiv.org/abs/2110.03843>
- 1427 Horne, K. 1986, PASP, 98, 609, doi: [10.1086/131801](https://doi.org/10.1086/131801)
- 1428 Huang, Y., Lee, K.-S., Shi, K., et al. 2021, arXiv e-prints,
 1429 arXiv:2104.11354. <https://arxiv.org/abs/2104.11354>
- 1430 Jung, I., Finkelstein, S. L., Livermore, R. C., et al. 2018,
 1431 ApJ, 864, 103, doi: [10.3847/1538-4357/aad686](https://doi.org/10.3847/1538-4357/aad686)
- 1432 Jung, I., Finkelstein, S. L., Dickinson, M., et al. 2020, ApJ,
 1433 904, 144, doi: [10.3847/1538-4357/abbd44](https://doi.org/10.3847/1538-4357/abbd44)
- 1434 Kelz, A., Jahn, T., Haynes, D., et al. 2014, Society of
 1435 Photo-Optical Instrumentation Engineers (SPIE)
 1436 Conference Series, Vol. 9147, VIRUS: assembly, testing
 1437 and performance of 33,000 fibres for HETDEX, 914775,
 1438 doi: [10.1117/12.2056384](https://doi.org/10.1117/12.2056384)
- 1439 Khostovan, A. A., Malhotra, S., Rhoads, J. E., et al. 2021,
 1440 MNRAS, 503, 5115, doi: [10.1093/mnras/stab778](https://doi.org/10.1093/mnras/stab778)
- 1441 Koekemoer, A. M., Faber, S. M., Ferguson, H. C., et al.
 1442 2011, ApJS, 197, 36, doi: [10.1088/0067-0049/197/2/36](https://doi.org/10.1088/0067-0049/197/2/36)

- ¹⁴⁴³ Kusakabe, H., Shimasaku, K., Ouchi, M., et al. 2018, PASJ, 70, 4, doi: [10.1093/pasj/psx148](https://doi.org/10.1093/pasj/psx148)
- ¹⁴⁴⁵ Lang, D., Hogg, D. W., & Mykytyn, D. 2016, The Tractor: Probabilistic astronomical source detection and measurement. <http://ascl.net/1604.008>
- ¹⁴⁴⁸ Lee, S.-K., Ferguson, H. C., Somerville, R. S., Wiklind, T., & Giavalisco, M. 2010, ApJ, 725, 1644, doi: [10.1088/0004-637X/725/2/1644](https://doi.org/10.1088/0004-637X/725/2/1644)
- ¹⁴⁵¹ Leja, J., Johnson, B. D., Conroy, C., van Dokkum, P. G., & Byler, N. 2017, ApJ, 837, 170, doi: [10.3847/1538-4357/aa5ffe](https://doi.org/10.3847/1538-4357/aa5ffe)
- ¹⁴⁵⁴ Leung, A. S., Acquaviva, V., Gawiser, E., et al. 2017, ApJ, 843, 130, doi: [10.3847/1538-4357/aa71af](https://doi.org/10.3847/1538-4357/aa71af)
- ¹⁴⁵⁶ Madau, P., & Dickinson, M. 2014, ARA&A, 52, 415, doi: [10.1146/annurev-astro-081811-125615](https://doi.org/10.1146/annurev-astro-081811-125615)
- ¹⁴⁵⁸ Malhotra, S., & Rhoads, J. E. 2004, ApJL, 617, L5, doi: [10.1086/427182](https://doi.org/10.1086/427182)
- ¹⁴⁶⁰ Marchi, F., Pentericci, L., Guaita, L., et al. 2019, A&A, 631, A19, doi: [10.1051/0004-6361/201935495](https://doi.org/10.1051/0004-6361/201935495)
- ¹⁴⁶² Martin, C. L., Dijkstra, M., Henry, A., et al. 2015, ApJ, 803, 6, doi: [10.1088/0004-637X/803/1/6](https://doi.org/10.1088/0004-637X/803/1/6)
- ¹⁴⁶⁴ Matthee, J., Sobral, D., Oteo, I., et al. 2016, MNRAS, 458, 449, doi: [10.1093/mnras/stw322](https://doi.org/10.1093/mnras/stw322)
- ¹⁴⁶⁶ Matthee, J., Sobral, D., Hayes, M., et al. 2021, MNRAS, 505, 1382, doi: [10.1093/mnras/stab1304](https://doi.org/10.1093/mnras/stab1304)
- ¹⁴⁶⁸ Miralda-Escudé, J. 1998, ApJ, 501, 15, doi: [10.1086/305799](https://doi.org/10.1086/305799)
- ¹⁴⁶⁹ Neufeld, D. A. 1991, ApJL, 370, L85, doi: [10.1086/185983](https://doi.org/10.1086/185983)
- ¹⁴⁷⁰ Ouchi, M., Ono, Y., & Shibuya, T. 2020, ARA&A, 58, 617, doi: [10.1146/annurev-astro-032620-021859](https://doi.org/10.1146/annurev-astro-032620-021859)
- ¹⁴⁷² Oyarzún, G. A., Blanc, G. A., González, V., Mateo, M., & Bailey, John I., I. 2017, ApJ, 843, 133, doi: [10.3847/1538-4357/aa7552](https://doi.org/10.3847/1538-4357/aa7552)
- ¹⁴⁷⁵ Papovich, C., Dickinson, M., & Ferguson, H. C. 2001, ApJ, 559, 620, doi: [10.1086/322412](https://doi.org/10.1086/322412)
- ¹⁴⁷⁷ Papovich, C., Finkelstein, S. L., Ferguson, H. C., Lotz, J. M., & Giavalisco, M. 2011, MNRAS, 412, 1123, doi: [10.1111/j.1365-2966.2010.17965.x](https://doi.org/10.1111/j.1365-2966.2010.17965.x)
- ¹⁴⁸⁰ Papovich, C., Shipley, H. V., Mehrtens, N., et al. 2016, ApJS, 224, 28, doi: [10.3847/0067-0049/224/2/28](https://doi.org/10.3847/0067-0049/224/2/28)
- ¹⁴⁸² Partridge, R. B., & Peebles, P. J. E. 1967, ApJ, 147, 868, doi: [10.1086/149079](https://doi.org/10.1086/149079)
- ¹⁴⁸⁴ Pentericci, L., Grazian, A., Fontana, A., et al. 2009, A&A, 494, 553, doi: [10.1051/0004-6361:200810722](https://doi.org/10.1051/0004-6361:200810722)
- ¹⁴⁸⁶ Pentericci, L., Grazian, A., Scarlata, C., et al. 2010, A&A, 514, A64, doi: [10.1051/0004-6361/200913425](https://doi.org/10.1051/0004-6361/200913425)
- ¹⁴⁸⁸ Ramsey, L. W., Sebring, T. A., & Sneden, C. A. 1994, Society of Photo-Optical Instrumentation Engineers (SPIE) Conference Series, Vol. 2199, Spectroscopic survey telescope project, ed. L. M. Stepp, 31–40, doi: [10.1117/12.176221](https://doi.org/10.1117/12.176221)
- ¹⁴⁹³ Reddy, N. A., Topping, M. W., Shapley, A. E., et al. 2021, arXiv e-prints, arXiv:2108.05363. <https://arxiv.org/abs/2108.05363>
- ¹⁴⁹⁶ Rhoads, J. E., Malhotra, S., Dey, A., et al. 2000, ApJL, 545, L85, doi: [10.1086/317874](https://doi.org/10.1086/317874)
- ¹⁴⁹⁸ Robertson, B. E., Ellis, R. S., Furlanetto, S. R., & Dunlop, J. S. 2015, ApJL, 802, L19, doi: [10.1088/2041-8205/802/2/L19](https://doi.org/10.1088/2041-8205/802/2/L19)
- ¹⁵⁰¹ Sanders, R. L., Shapley, A. E., Kriek, M., et al. 2018, ApJ, 858, 99, doi: [10.3847/1538-4357/aabcbd](https://doi.org/10.3847/1538-4357/aabcbd)
- ¹⁵⁰³ Santos, S., Sobral, D., Matthee, J., et al. 2020, MNRAS, 493, 141, doi: [10.1093/mnras/staa093](https://doi.org/10.1093/mnras/staa093)
- ¹⁵⁰⁵ Scarlata, C., Colbert, J., Teplitz, H. I., et al. 2009, ApJL, 704, L98, doi: [10.1088/0004-637X/704/2/L98](https://doi.org/10.1088/0004-637X/704/2/L98)
- ¹⁵⁰⁷ Shapley, A. E., Steidel, C. C., Pettini, M., & Adelberger, K. L. 2003, ApJ, 588, 65, doi: [10.1086/373922](https://doi.org/10.1086/373922)
- ¹⁵⁰⁹ Shimakawa, R., Kodama, T., Shibuya, T., et al. 2017, MNRAS, 468, 1123, doi: [10.1093/mnras/stx091](https://doi.org/10.1093/mnras/stx091)
- ¹⁵¹¹ Sobral, D., Santos, S., Matthee, J., et al. 2018, MNRAS, 476, 4725, doi: [10.1093/mnras/sty378](https://doi.org/10.1093/mnras/sty378)
- ¹⁵¹³ Steidel, C. C., Erb, D. K., Shapley, A. E., et al. 2010, ApJ, 717, 289, doi: [10.1088/0004-637X/717/1/289](https://doi.org/10.1088/0004-637X/717/1/289)
- ¹⁵¹⁵ Trainor, R. F., Strom, A. L., Steidel, C. C., et al. 2019, ApJ, 887, 85, doi: [10.3847/1538-4357/ab4993](https://doi.org/10.3847/1538-4357/ab4993)
- ¹⁵¹⁷ Vargas, C. J., Bish, H., Acquaviva, V., et al. 2014, ApJ, 783, 26, doi: [10.1088/0004-637X/783/1/26](https://doi.org/10.1088/0004-637X/783/1/26)
- ¹⁵¹⁹ Weiss, L. H., Bowman, W. P., Ciardullo, R., et al. 2021, ApJ, 912, 100, doi: [10.3847/1538-4357/abedb9](https://doi.org/10.3847/1538-4357/abedb9)
- ¹⁵²¹ Wold, I. G. B., Barger, A. J., & Cowie, L. L. 2014, ApJ, 783, 119, doi: [10.1088/0004-637X/783/2/119](https://doi.org/10.1088/0004-637X/783/2/119)
- ¹⁵²³ Xue, Y. Q., Luo, B., Brandt, W. N., et al. 2016, ApJS, 224, 15, doi: [10.3847/0067-0049/224/2/15](https://doi.org/10.3847/0067-0049/224/2/15)
- ¹⁵²⁵ York, D. G., Adelman, J., Anderson, John E., J., et al. 2000, AJ, 120, 1579, doi: [10.1086/301513](https://doi.org/10.1086/301513)

1527

APPENDIX

1528 A. MODEL-DEPENDENCE OF MEASURED GALAXY PROPERTIES

1529 Bayesian approaches to SED fitting, like the one implemented in BAGPIPES provide robust constraints on the
 1530 parameter uncertainties and their interdependence, but the model chosen for comparison to the data (as well as the
 1531 chosen priors) determines the accuracy of those estimates. In other words, an inaccurate model yields inaccurate
 1532 measurements of galaxy properties. Many galaxy SED fitting studies have shown that model choices, such as the SFH,
 1533 systematically impact the measured galaxy properties (see Conroy 2013 for review).

1534 To test the robustness of our results to different modeling choices, we performed an additional analysis of our entire
 1535 sample using an alternate model. We did not seek to find a more (or less) accurate model; we simply wanted a different
 1536 model to determine if the median properties or correlations between Ly α emission and galaxy properties changed. To
 1537 this end, we adopted a constant SFH parametrization as well as the dust absorption model of Charlot & Fall 2000.
 1538 The constant SFH required two parameters: the time when star formation began and the constant star formation rate.
 1539 For dust attenuation, we adopted the recipe given in Charlot & Fall (2000) by using an absorption curve proportional
 1540 to $\lambda^{-0.7}$, and a factor of three reduction in the dust extinction normalization for stellar populations older than 10^7
 1541 years to account for the dispersal of stellar birth clouds. The authors found this recipe to match the absorption of
 1542 stellar continuum and nebular emission for nearby starburst galaxies very well, and the differential extinction toward
 1543 young stars differs markedly from the treatment by Calzetti et al. (1994) used in our “fiducial” model presented above.
 1544 Figure 17 shows the distribution of LAE properties measured using the alternate model compared with the fiducial
 1545 model. The sample median stellar mass increased by 0.1 dex, as did the median SFR. These two changes do not
 1546 affect our results or interpretation significantly. The median dust dropped from $A_V = 0.30$ to 0.17, a fairly substantial
 1547 change, but not unusual given the common factors of \sim a few discrepancies between different models and SED-fitting
 1548 codes (see Leja et al. 2017). Nonetheless, the correlations between galaxy properties and $W_\lambda(\text{Ly}\alpha)$ remained unaffected
 1549 by the model modifications, as shown in Figure 18. Stellar mass and SFR correlated strongly and negatively with Ly α
 1550 emission strength, while other parameters, like dust extinction, continued to show no significant correlations.

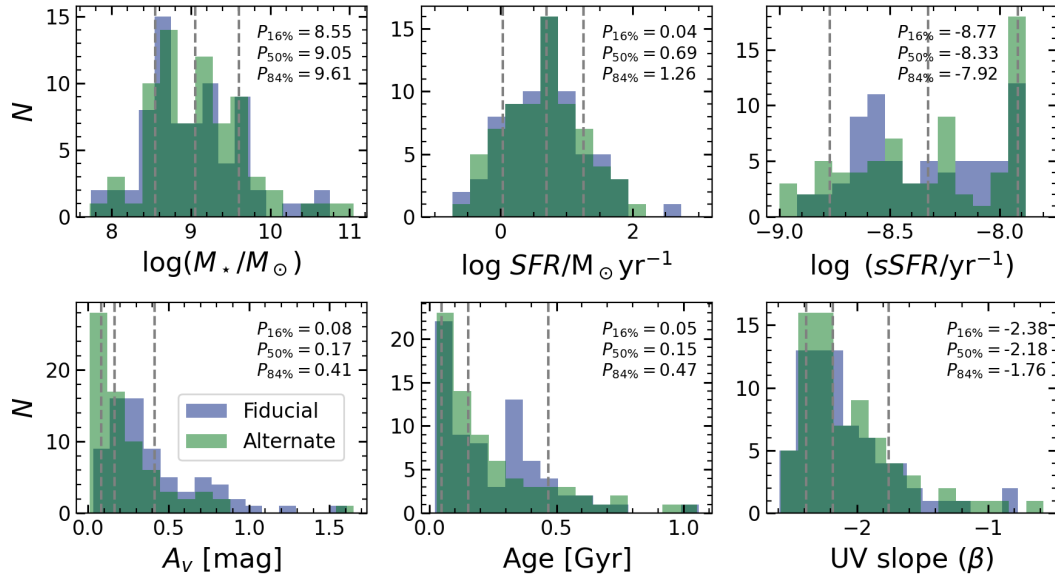


Figure 17. Comparison of galaxy properties as measured using our “fiducial” model (light blue) versus our “alternate” model (sea green). The 16th, 50th, and 84th percentiles calculated using the alternate model are indicated by vertical dashed grey lines, and their values are indicated with text. The distributions are consistent, save for dust extinction (A_V), which has lower values by a factor of ~ 2 for the alternate model.

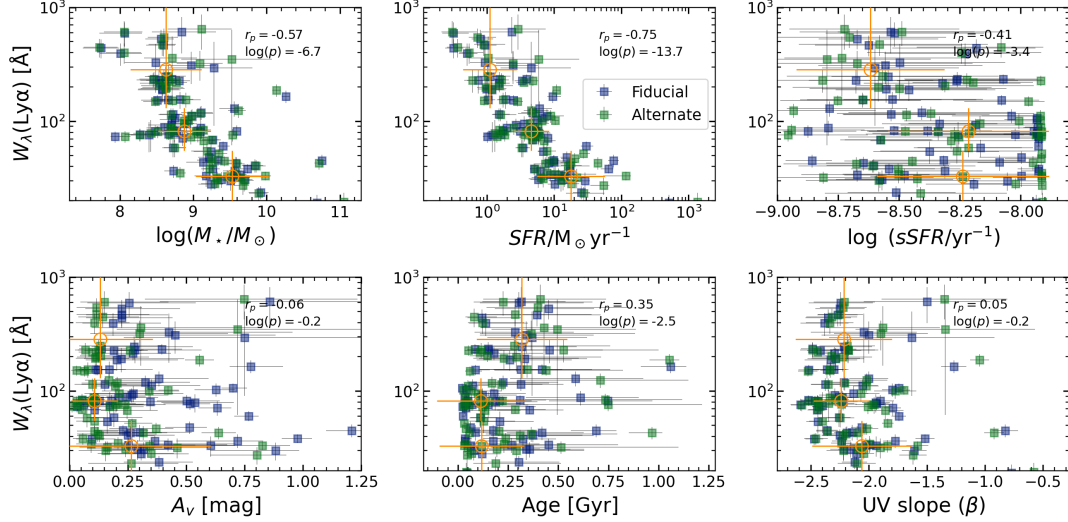
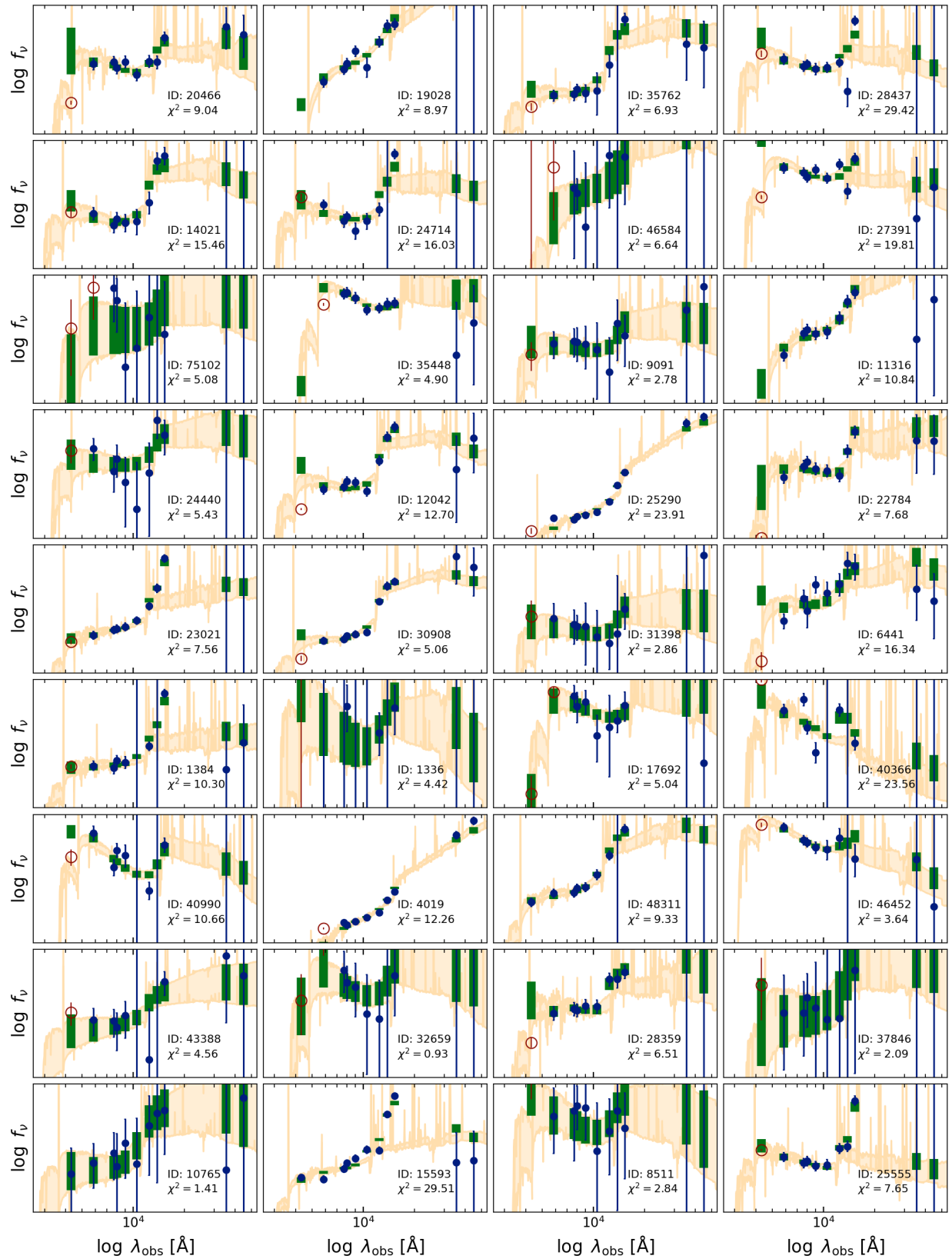


Figure 18. Comparison of correlations between $W_{\lambda}(\text{Ly}\alpha)$ and galaxy properties as measured using our “fiducial” model (light blue) versus our “alternate” model (sea green). Binned values from the alternate model are indicated as open gold circles. The correlations presented in §4.3 appear robust when different models are adopted.

1551

B. IMAGING, EMISSION LINES, AND SED FITS FOR LAES IN THIS STUDY

1552 In this section, for all 72 LAEs in our sample, we present *HST* imaging cutouts in Figure 21 showing the sources
 1553 and any neighbors, the HETDEX Ly α emission line detections in Figure 20, and the SED fits with BAGPIPES (Carnall
 1554 et al. 2018) used to measure physical properties in Figure 19.



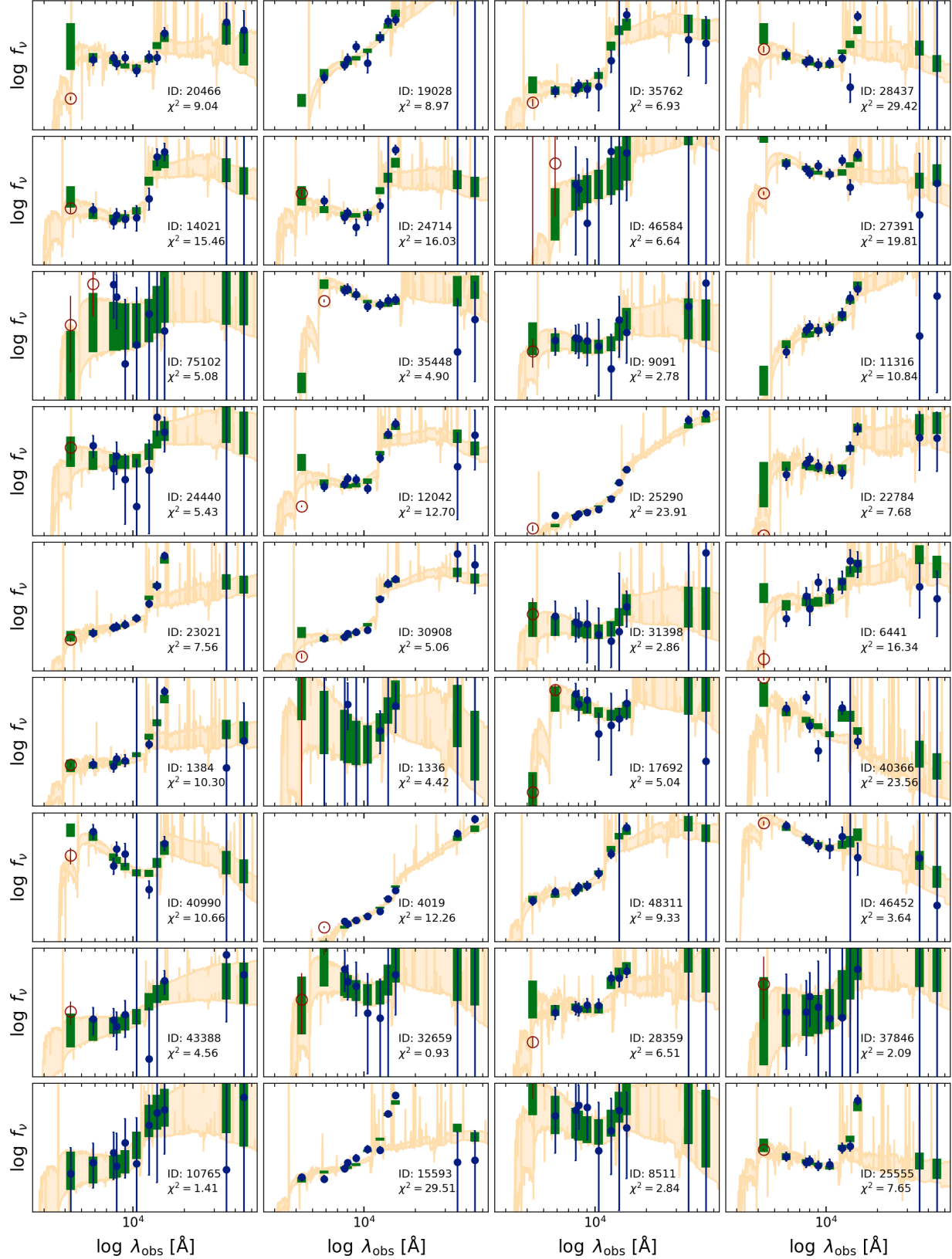


Figure 19. All SED fits for LAEs in the sample (see Figure 9 for a description of the plots). The χ^2 value for each fit is also given with text.

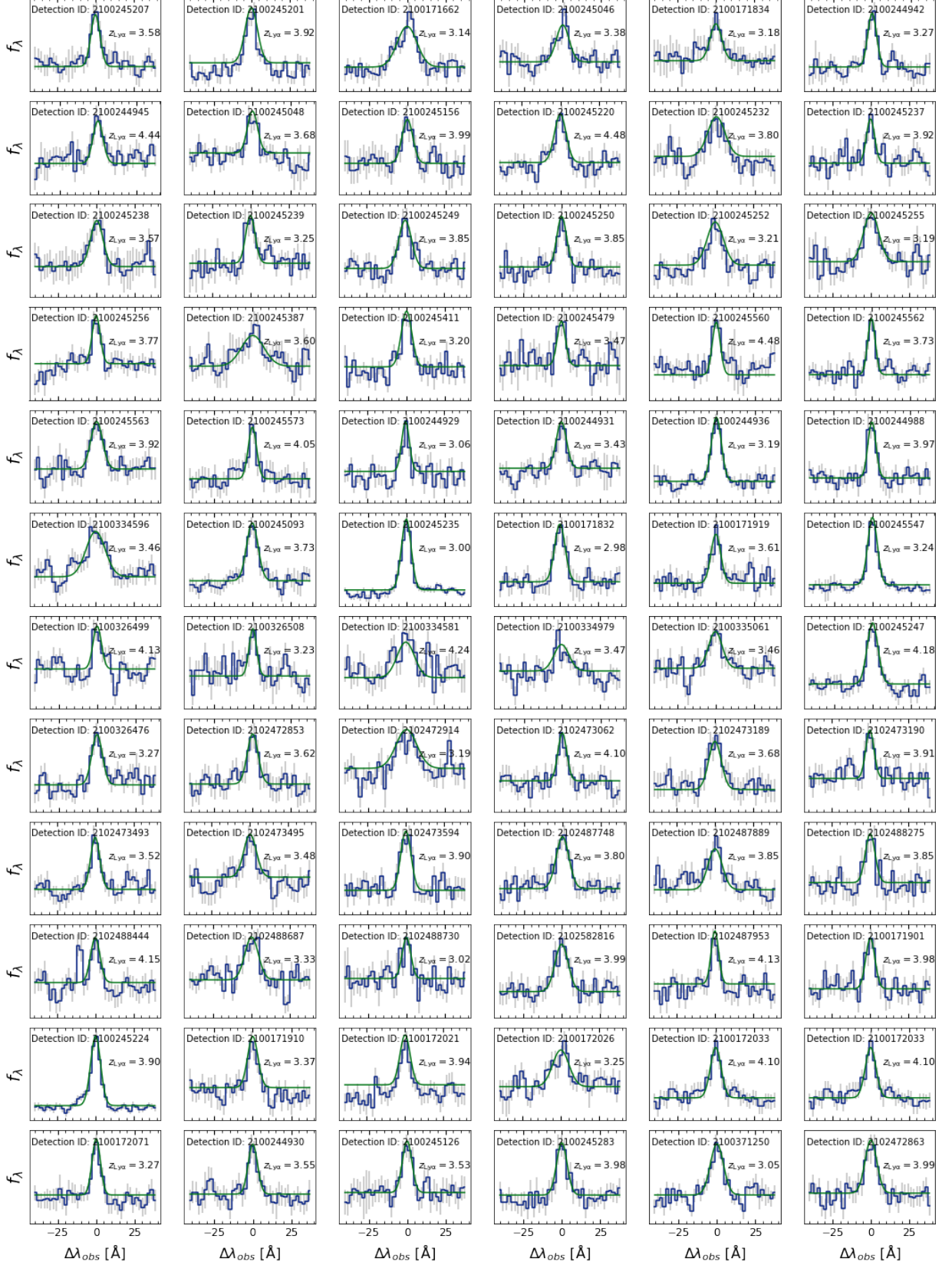


Figure 20. All emission line detections from the HETDEX Survey for LAEs in the sample. The observed data are indicated by the blue lines with grey error bars. A Gaussian model fit to the data is shown in green. The x-axis is scaled in Angstroms relative to the line center.

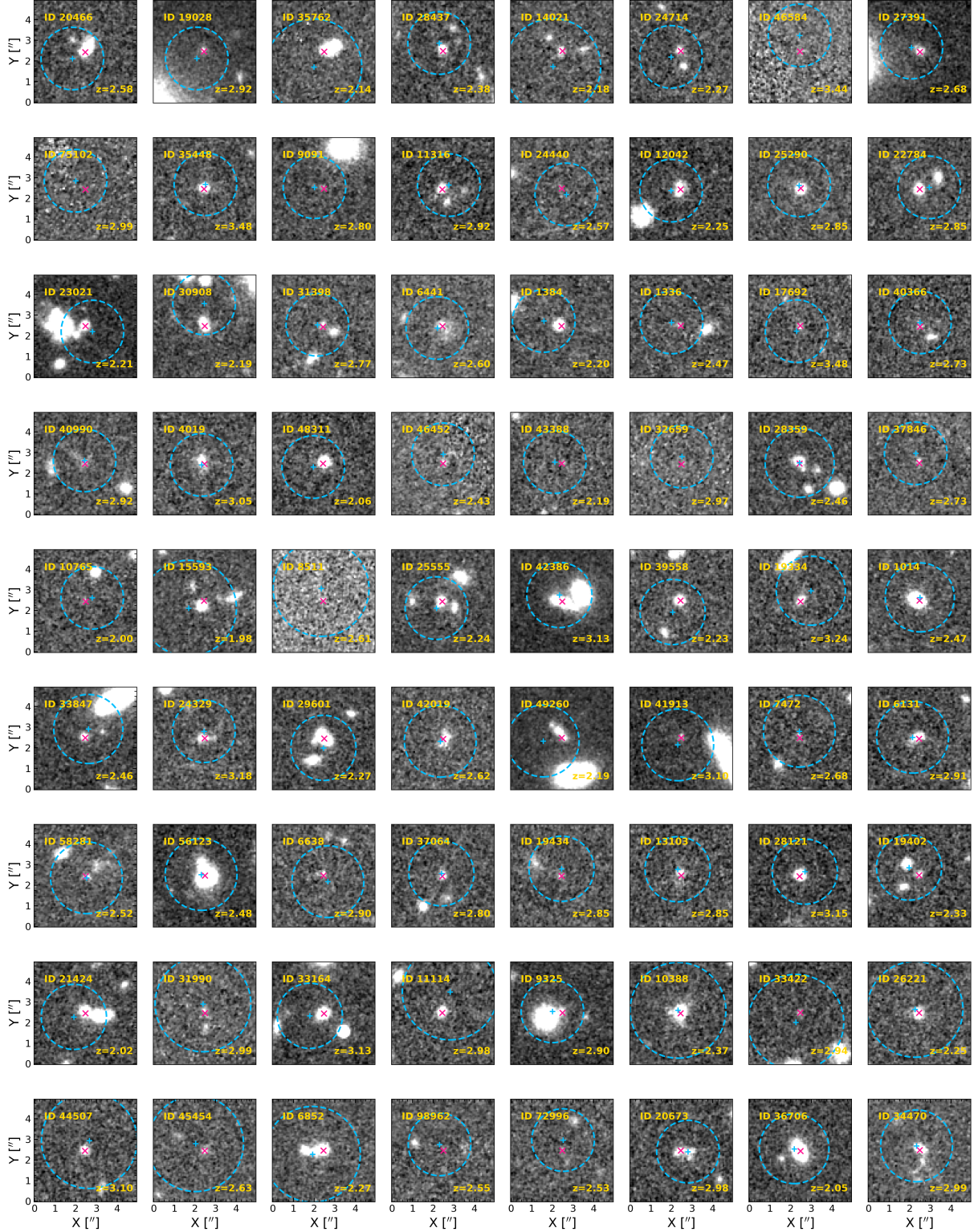


Figure 21. All *HST* F160W (*H*-band) images of LAEs in the sample. Each cutout shows a $5'' \times 5''$ image centered on each galaxy in our sample. The galaxy centroid is indicated with a pink diamond, and the HETDEX detection position and PSF FWHM are indicated by a light blue cross and dashed circle, respectively. We also include object IDs and redshifts with text.